



NTNU – Trondheim
Norwegian University of
Science and Technology

Improved Induced Diode Photodetectors by Increased Fixed Charge in PECVD Amorphous Silicon Nitride

Molly Strimbeck Bazilchuk

Nanotechnology

Submission date: June 2014

Supervisor: Jostein Grepstad, IET

Co-supervisor: Jarle Gran, Justervesenet

Norwegian University of Science and Technology
Department of Electronics and Telecommunications

This work was performed as the final part of a master's degree in nanoelectronics at the Norwegian University of Science and Technology (NTNU). The research question was posed by Justervesenet (the Norwegian Metrology Service), whereas all experimental work was carried out at the Solar Cell Laboratory at the Institute for Energy Technology (IFE) in Kjeller, Norway.

A number of people were instrumental in the completion of this thesis. First of all, I would like to thank my supervisor Jarle Gran at Justervesenet. I left every meeting with you feeling encouraged, and with a new sense of direction and purpose. I would also like to thank Jostein Grepstad, my supervisor at NTNU, for answering my emails wherever you were in the world and for teaching me to take nothing for granted. I learned so much from you even though we have worked together from two different cities.

Next I would like to thank the good people at the Institute for Energy Technology, who allowed me to use their laboratories and badger their engineers and postdocs for the better part of a year. Without their help and equipment I would never have been already to produce such great results. I would especially like to thank Erik Marstein and Halvard Haug, who supervised my practical work. Erik sees the positive side of every failed experiment, and always had a thousand new ideas. You are an inspiration to us all. Halvard was my walking encyclopedia, and could always dig up exactly the theory I needed to explain my data. I also like to thank Chang Chuan You and Ørnulf Nordseth for help processing samples and instrument training, and Josefine Selj for fitting my ellipsometric data.

I would also like to dedicate this work to my mom and dad, who have always said I could do whatever I wanted as long as I worked hard. I think they may have been right.

Finally I would like to thank the world's most patient Audun. Thank you for putting up with endless babbling about electrons, defect states and CV characterization at the dinner table. Probably you'll never read this thesis, but you know most of the contents anyway.

Abstract

The predictable quantum efficient detector (PQED) is a cheaper, more practical alternative to the current radiometric primary standard, the cryogenic radiometer. The PQED is made of an induced diode, a rectifying junction based on a positively charged dielectric film which induces an n-type inversion layer on a p-type silicon substrate. Increasing the fixed charge Q_f in the dielectric has been theoretically predicted to improve the quantum efficiency of the diode by decreasing the surface recombination velocity (SRV) at the dielectric-silicon interface, as well as improving the performance of the diode at high intensities. In this work, we propose the replacement of silicon oxide (SiO_x) with silicon nitride (SiN_x) as the inversion-inducing dielectric layer as a means of increasing Q_f .

Amorphous PECVD SiN_x has been shown to have a significantly higher Q_f than thermally grown SiO_x . A sixfold increase of Q_f in SiN_x by means of charge injection via bias soaking has also been demonstrated. The dielectric ideality of the nitride increases with the atomic nitrogen concentration x , and a high- x film has shown superior charge retention properties. The absorption in the high- x film is far less than 1 % in the applicable wavelength ranges, but is larger in the low- x film. The impact of Q_f on the SRV has been experimentally demonstrated, and may be fit to the extended SRH theory with the inclusion of a sub-surface damage term. Finally, it has been demonstrated that the aluminium contacts deposited for the purpose of charging the SiN_x may be chemically removed while the injected charge remains. SiN_x has thus been shown to be an interesting candidate for the PQED application.

Table of Contents

Abstract	i
Table of Contents	iv
List of Tables	v
List of Figures	viii
Abbreviations	1
1 Introduction	3
1.1 Goals	4
1.2 Outline	5
2 Theory	7
2.1 Photodetectors and the PQED	7
2.1.1 Cryogenic Radiometer	8
2.1.2 Quantum Detectors	9
2.2 Contributions to the Quantum Deficiency	10
2.2.1 Reflection	11
2.2.2 Absorption	11
2.2.3 Transmission	12
2.2.4 Free-Carrier Absorption	13
2.2.5 Generation Current	14
2.2.6 Bulk Recombination	14
2.2.7 Surface Recombination	16
2.3 The Induced Diode	17
2.3.1 Band Structure	17
2.3.2 Charge Balance	18
2.3.3 Advantages of Induced Diodes	20
2.3.4 Effects of Increasing the Fixed Charge	22

2.4	Properties of Silicon Oxide and Silicon Nitride	25
2.4.1	Silicon Oxide	25
2.4.2	Silicon Nitride	26
3	Introduction to Characterization Methods	29
3.1	Capacitance-Voltage Characterization	29
3.1.1	Ideal MIS Capacitors	30
3.1.2	Real MIS Capacitors	33
3.2	Measuring Lifetime	35
3.2.1	Quasi-Steady State and Quasi-Transient Lifetime Measurements .	36
3.2.2	Photoluminescence Imaging	37
4	Experimental Methods	39
4.1	Sample Fabrication	39
4.1.1	Plasma-Enhanced Chemical Vapor Deposition (PECVD)	39
4.1.2	Electrode Metallization	41
4.2	Characterization	42
4.2.1	Ellipsometry	42
4.2.2	Photoluminescence Imaging	44
4.2.3	Quasi Steady-State Photoconductance Decay	44
4.2.4	Capacitance-Voltage Set-up	44
5	Results and Discussion	47
5.1	Initial Characterization	47
5.1.1	Optical Characterization	47
5.1.2	CV characterization	49
5.1.3	Initial lifetime characterization	52
5.2	Charge Injection Analysis	55
5.2.1	Charging Injection Study	55
5.2.2	SRV-Fixed Charge Analysis	59
5.2.3	Electrode removal	63
6	Conclusion	65
7	Suggestions for further work	67
	Bibliography	68
	Appendix	73

List of Tables

4.1	<i>Characteristics of the wafers.</i>	39
4.2	<i>PECVD deposition parameters for the two types of nitride film deposited in the sample set.</i>	40
4.3	<i>The characteristics of the sample set.</i>	40
5.1	<i>Ellipsometrically measured thicknesses and refractive indices of the samples.</i>	47
5.2	<i>Percentage of electrodes without leakage, average Q_f and the standard deviation of Q_f statistically calculated over the 56 electrodes of each sample.</i>	52
5.3	<i>The effective carrier lifetimes at $\Delta n = 10^{15}$ as measured using QSSPC.</i>	53
5.4	<i>The average SRV based on QSSPC measurements.</i>	53
5.5	<i>The fit parameters for the theoretical model of $SRV(Q_f)$ given in equation 5.1.</i>	63
5.6	<i>The effective lifetimes before and after electrode removal.</i>	64

List of Figures

2.1	<i>The workings of a cryogenic radiometer</i>	8
2.2	<i>Schematic of the trap detector structure designed during the qu-Candela project.</i>	11
2.3	<i>The relative intensity of light through a silicon wafer at different wavelengths.</i>	13
2.4	<i>Recombination mechanisms, from left to right: radiative, Auger and SRH.</i>	15
2.5	<i>A cross-section of the original PQED induced diode design.</i>	17
2.6	<i>Band structure of an induced diode.</i>	18
2.7	<i>A one-dimensional model of the charge distribution in a self-induced diode.</i>	18
2.8	<i>The depletion width W_{\max} as a function of the wafer doping N_a.</i>	20
2.9	<i>The internal quantum deficiency of a PN diode and an induced diode, as modelled in PCID.</i>	21
2.10	<i>The surface recombination velocity at the SiN_x-Si interface as a function of the fixed charge.</i>	23
2.11	<i>The IQD as a function of the SRV for several wavelengths and fixed charge densities.</i>	24
2.12	<i>The SRV at the SiN_x-Si interface as a function of Q_f.</i>	25
3.1	<i>Band diagrams of accumulation, depletion and inversion in an ideal p-type MIS capacitor.</i>	31
3.2	<i>An ideal CV sweep of a MIS capacitor with no fixed charge, at low frequency and with a fixed charge Q_f.</i>	33
3.3	<i>Circuit diagram of a MIS capacitor with series resistance.</i>	35
3.4	<i>A general schematic showing a PL set-up.</i>	38
4.1	<i>The defects seen in the a-Si deposited on all of the wafers.</i>	41
4.2	<i>Images of the two sample types.</i>	42
4.3	<i>The J.A. Woollam variable angle spectroscopic ellipsometer.</i>	43
4.4	<i>The ellipsometric fit for Δ of sample 1.</i>	43
4.5	<i>The probe station used to perform CV measurements.</i>	45

5.1	<i>The fraction of incident light absorbed in the SiN_x films as a function of the wavelength λ.</i>	48
5.2	<i>A typical initial CV sweep of sample 1.</i>	50
5.3	<i>A typical initial CV sweep of sample 2.</i>	50
5.4	<i>A typical initial CV sweep of sample 3.</i>	51
5.5	<i>A typical CV sweep of a partially failed electrode.</i>	52
5.6	<i>Calibrated PL images of the lifetime samples.</i>	54
5.7	<i>The charge Q_f measured as a function of the biasing time at -30V.</i>	55
5.8	<i>The charge Q_f measured on the samples after biasing for 70 s at a soaking bias.</i>	56
5.9	<i>Stability of the induced charge Q_f measured on the samples that had been charged to saturation at -30 V and then measured successively for up to 50 days.</i>	57
5.10	<i>A typical CV sweep of sample 1 during the charge stability study.</i>	58
5.11	<i>Post-bias CV sweeps with corresponding PL images showing the increase in Q_f.</i>	60
5.12	<i>τ_{eff} as a function of Q_f as measured by dual the CV/PL characterization for three electrodes of the CV/PL wafer of sample 2.</i>	61
5.13	<i>The best and worst case SRVs of each of the three electrodes measured, fitted using extended SRH formalism and the sub-surface damage theory.</i>	62
5.14	<i>Calibrated PL images before and after electrode removal.</i>	64

Abbreviations

CV	=	Capacitance-voltage
EHP	=	Electron-hole pair
IQD	=	Internal quantum efficiency
MIS	=	Metal-insulator-semiconductor capacitor
PECVD	=	Plasma-enhanced chemical vapor deposition
PL	=	Photoluminescence
PQED	=	Predictable quantum efficient detector
QE	=	Quantum efficiency
QD	=	Quantum deficiency
QSSPC	=	Quasi-steady-state photoconductance
SRH	=	Shockley-Read-Hall
SRV	=	Surface recombination velocity
VASE	=	Variable angle spectroscopic ellipsometer

Introduction

The ability of photons to transmit information is of fundamental interest for an expansive range of technologies. From fiberoptics and telecommunications to laser printers and barcode scanners, the applications of photonics can be seen everywhere. For a number of applications, *photodetectors* are necessary in order to accurately measure optical power. The charge-coupled devices (CCD) used in digital photography are photodetectors, as are arrays of photodiodes that are used as position detectors. A number of scientific applications, such as solar cell characterization, require photodetectors. Although a photodetector may measure photons of any wavelength, of principle interest here is the detection of visible light, with wavelengths of 400 - 800 nm.

In essence, a photodetector transforms incident optical power to a signal. *Thermal detectors* convert the photon energy to heat and then measure the resulting temperature change. *Quantum detectors* convert photons to excited electron-hole pairs, which are measured as electrical current in an external circuit. The current is directly proportional to the number of incident photons whose energy is greater than the semiconducting bandgap. A silicon-based detector has a bandgap of $E_g = 1.12\text{eV}$, which will allow the detection of all wavelengths of visible light.

Calibration, or comparing a device to some reliable standard, is indispensable for high accuracy measurements. Furthermore, the existence of an accurate calibration standard allows other photodetectors to perform more optimally. This work deals with the science and fabrication of high-accuracy photodetectors for use in standard calibration purposes.

In metrology, a primary standard is an artifact which itself does not require calibration. In current radiometry, the measurement of visible light, the primary standard is the cryogenic radiometer. This detector has a number of disadvantages, such as cost and dynamic range, and there has been a movement in recent years to create a new type of silicon-based primary standard.

In 2008, the EU project Quantum Candela commenced, aiming to develop new standards for photon metrology [3]. As a part of this project, work began to develop a *predictable quantum efficient detector (PQED)* that could be used to measure optical power with uncertainties as low as 1 ppm. In 2013, the EU project NEWSTAR (New Standards in Ra-

diometry) started, continuing the promising work on the PQED [39, 30, 18]. Justervesenet (the Norwegian Metrology Service) has played a central role in both of these projects, and this work is an extension of their work.

The current design of the PQED is based on an *induced diode*. Fixed, positive charges are found in certain dielectrics, notably silicon oxide and silicon nitride, when deposited on silicon. When a thin film of either of these dielectrics is deposited onto a p-type silicon wafer, the positive charges in the dielectric repel the mobile holes and attract electrons in the bulk, creating an n-type inversion layer near the dielectric-silicon interface. The induced diode was introduced by Hansen in 1978 [20]. This type of diode became of interest the metrology community after Geist et al. [14] published work suggesting that it could be used in a detector that could be at least as accurate as the cryogenic radiometer.

Increasing the surface density of fixed charge Q_f in the dielectric has been predicted to increase the effective charge carrier lifetime in the device and hence improve the quantum efficiency of the device. Furthermore, an increased Q_f will improve the performance of the PQED at higher optical powers. The principle goal of this work is to investigate methods to increase Q_f .

The PQED developed in the Quantum Candela project was made with thermally grown silicon oxide (SiO_x) as the inverse-inducing dielectric. The intrinsic fixed charge in amorphous PECVD silicon nitride (SiN_x) is an order of magnitude greater than that in SiO_x . It has therefore been decided to investigate the possibility of replacing SiO_x with SiN_x in a future PQED, as well as the possibility of further increasing Q_f in the SiN_x layer.

There are many ways of potentially increasing Q_f in a dielectric, but in this work we focus on injecting charges into the SiN_x film by applying a soaking bias across the SiN_x -Si system. Charge injection in nitride is a well-known phenomenon [26, 34, 10, 49], but has not previously been investigated in the context of detector applications. A deeper understanding of methods of manipulation of fixed charges in dielectrics is also of fundamental interest in other areas, such as solar cell passivation.

1.1 Goals

The principle goal of this work is to investigate methods of increasing the magnitude of the positive surface density of fixed charge in SiN_x , and confirming its suitability for the PQED application. The ideal requirements for the SiN_x may be summarized as follows:

- The practical maximum of the fixed charge Q_f in SiO_x is $7 \times 10^{11} \text{ cm}^{-2}$. 'Increased charge' is thus defined as Q_f than this value.
- Q_f must be stable, and should not degrade significantly over time or under the influence of light or temperature fluctuations.
- The SiN_x layer should be completely transparent in the $\lambda = 400 - 800 \text{ nm}$ range. By this we mean the absorptions in the film should ideally be quantified to less than 0.01%.
- The dielectric should act as a passivating layer in the detector, meaning that a minimum of interface states should be introduced as a result of increasing Q_f . This

will be quantified by examining the charge carrier lifetime in the device, which should increase as a function of increased charge.

1.2 Outline

Chapter 2 introduces important concepts in photodetectors and uncertainty in radiometry, and continues with a description of the different loss mechanisms which cause non-ideal behavior in the PQED. Next the induced diode structure is discussed in detail. The properties and origins of Q_f in SiO_x and SiN_x are then compared, followed by a review of possible methods of increasing Q_f .

Chapter 3 introduces the central measurement techniques used to determine fixed charge in dielectrics and characterize lifetime.

Chapter 4 summarizes the experimental parameters used in fabricating the samples, and describes the various set-ups used to characterize the samples.

Chapter 5 summarizes and discusses the experimental results. First, preliminary ellipsometric, lifetime and electrical characterizations are presented. Next, a more in-depth study of the manipulation of the fixed charges in silicon nitride is presented.

Chapter 6 concludes with the findings of this work, while *Chapter 7* presents suggestions for further work on this topic.

Theory

This chapter outlines the fundamental theory needed to understand the fabrication and operation of precise, silicon-based photodetectors.

This work is part of the development of a novel radiometric calibration standard. Section 2.1 provides a brief overview of the requirements for a primary radiometric standard and the ways in which the accuracy and uncertainty of a photodetector may be quantified.

Section 2.2 discusses the factors that contribute to losses in accuracy in the predictable, quantum efficient detector (PQED). All of these contributions must be minimized to achieve the best possible photodetector. The remainder of this work, however, focuses mainly on losses to recombination (as described in sections 2.2.6 and 2.2.7).

In section 2.3 the induced diode structure from which the PQED is made is discussed. The induced diode is not commonly used in devices, and therefore the system is described in depth. The text discusses the reasons this structure has been selected and how this work attempts to improve it.

Finally, section 2.4 discusses Q_f present in SiO_x and SiN_x , which provides the physical basis for the induced diode structure.

2.1 Photodetectors and the PQED

A photodetector is a device that measures optical power by providing a signal proportional to the incident photon flux. In this thesis, the range of interest is visible light, or $\lambda = 400 - 800\text{nm}$. The goal of the EU project NEWSTAR is to develop a new calibration standard for optical power in this spectral range, as well as testing it in different applications by building the primary standard into the application. In order for a detector to perform as a primary calibration standard, it must be absolute, meaning that the measured quantity can be directly expressed by fundamental constants or other SI units.

The PQED is a detector developed in the recent Qu-Candela project [39, 30]. By predictable, we mean that all of the losses, both external and internal, can be accurately measured or modelled so that the response of the detector can be predicted. The device should also have a high quantum efficiency, or conversion rate of photons to electrons, in

order to accurately quantify incident power, a concept which will be further explored in section 2.1.2.

The PQED is designed to be used at incident optical powers of 1 - 100 μW . This range could be extended further in either direction if the detector can be shown to be linear and accurate for a higher dynamic range. The detector is $1 \times 2 \text{ cm}$ in area, and the area of incidence is 1 cm^{-2} .

2.1.1 Cryogenic Radiometer

The current radiometric calibration standard is the cryogenic radiometer, which is a thermal detector. As the name suggests, the set-up is operated at low temperatures, specifically around 4 K, requiring a helium cryostat. The device has a cavity in which incident light is absorbed. The cavity is designed to absorb 99.9998% of incident light. The incident light heats the cavity, and the increase in temperature is measured with a set of thermometers.

The temperature change in the detector during alternate radiative and electrical heating cycles is recorded. The optical power required to heat the detector is thus compared to the electrical power required to heat the detector for a given wavelength. The temperature change is compared to a reference temperature in a heat sink [29]. Figure 2.1 shows a schematic of an accurate cryogenic radiometer, taken from [15].

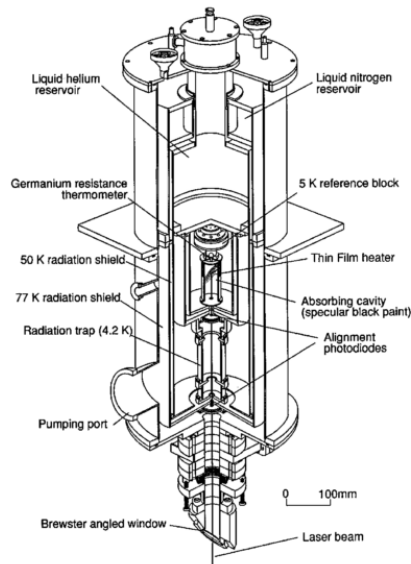


Figure 2.1: *The workings of a cryogenic radiometer*

Although it attains an uncertainty of 200 ppm, the cryogenic radiometer is not an easy or fast instrument to use. The use of a helium cryostat increases measurement time and complexity, as well as being costly. In addition, a certain stabilization time is required between successive electrical and optical heating cycles. Calibrating a device for a range of wavelengths directly against the cryogenic radiometer can thus take a long time.

2.1.2 Quantum Detectors

An alternative to thermal detectors, and hence the cryogenic radiometer, is the quantum detector. A quantum detector produces an electric current that can be related to the incident power. An ideal quantum detector produces one charge carrier in the external circuit for every incident photon with energy greater than the semiconducting bandgap, $\frac{hc}{\lambda} > E_g$.

Quantum Efficiency

The quantum efficiency η is the ratio between charge carriers detected in the external circuit and the number of incident photons. An ideal quantum detector is defined as having a quantum efficiency $\eta = 1$.

The quantum efficiency may be split into internal and external contributions. The external quantum efficiency (EQE) is synonymous with the quantum efficiency. The internal quantum efficiency (IQE) is the ratio of charge carriers measured in the external circuit to photons that penetrate the surface of the detector. The IQE thus ignores any external losses to reflection. For convenience, the concept of quantum deficiency (QD) is sometimes used; this refers to the opposite of the quantum efficiency, so that $QD = 1 - QE$.

The initial PQED had a external quantum deficiency of around 50 ppm at 300 K [30]. The relative standard uncertainty of the measurements was less than 100 ppm, and the detector was shown to be linear across 6 orders of magnitude of incident optical power [30]. Ensuring a high quantum efficiency improves the *sensitivity* of the detector.

Responsivity and Predictability

The responsivity \mathfrak{R} of a detector is defined as the constant of proportionality between the the incident optical power P and the current generated in the external circuit i_p , referred to henceforth as the photocurrent. The photocurrent is thus given by the equation[43]:

$$i_p = \mathfrak{R}P \quad (2.1)$$

The optical power incident on the diode can be expressed as $P = h\nu\Phi$, where ν is the frequency of the incident light and Φ is the incident photon flux. For an ideal quantum detector, the photocurrent will be proportional to the incident photon flux, $i_p = e\Phi = \frac{eP}{h\nu}$. Inserting these two definitions into equation 2.1 and rearranging yields the responsivity of an ideal quantum detector as the following equation:

$$\mathfrak{R} = \frac{e\lambda}{hc} \quad (2.2)$$

The responsivity must be known in order to determine the optical power for a given wavelength¹. A non-ideal quantum detector will have a responsivity that deviates from the ideal, but it can be expressed based on losses in the detector by the following equation[39]:

$$\mathfrak{R}(\lambda) = \frac{e\lambda}{hc} [1 - \delta(\lambda)][1 - \rho(\lambda)] \quad (2.3)$$

¹Calibrations are performed based on a known wavelength, as might be obtained with a laser.

where δ are the internal losses after the photons have penetrated the surface of the detector or the internal quantum deficiency and ρ are the external losses through reflection off the surface of the detector. The external quantum deficiency is given by the sum of these two factors, $\text{EQE} = \rho + \delta$.

The accuracy in the correlation between incident power and measured current hinges on the accurate determination of the responsivity. This is where the importance of the PQED being *predictable* becomes apparent. Loss mechanisms must be predicatable in order to determine the corrected responsivity.

If an uncertainty of 10 ppm can be achieved in the responsivity of the PQED, it may be used to verify the fundamental constants e and h via equation 2.3.

Photodiodes

In principle, any rectifying junction may function as a photodiode and hence a quantum detector. Traditionally, photodiode detectors are made using a p-n or p-i-n junction. *Electron-hole pairs (EHP)* are collected in the depletion region of these junctions. It is thus advantageous to maximize the size of the depletion region in order to achieve a high QE. The intrinsic region in a p-i-n junction is one method of maximizing the depletion region. The PQED employs the rather novel induced diode structure, which will be discussed in detail in section 2.3, to this end. The photodiodes are operated in reverse bias so as to maximize the size of the depletion region, which maximizes the effective collection region in the diode.

In an unbiased photodiode, series resistance due to the bulk semiconductor creates a voltage opposing the built-in voltage for high currents. This creates signal non-linearity in incident optical power. By reverse biasing the photodiode, the series resistance is counteracted and the linearity is improved.

2.2 Contributions to the Quantum Deficiency

In an ideal photodiode, a photon will penetrate the surface of the device and excite an EHP. The EHP will then be separated by the electric field across the junction, and move through the external circuit connected to the diode as current. A quantum efficiency of unity requires every photon with energy larger than the semiconducting bandgap to create an electron in the external circuit.

Many factors hinder an incident photon in contributing to the photocurrent. This section explores the possible ways in which a photon can fail to create an electron in the external circuit, as well as mechanisms that cause false current (gain). All of the mechanisms are discussed with reference to silicon as this is the semiconductor of choice for the PQED. Geist [14] performed a theoretical, quantitative study of the contributions to the quantum deficiency on which the uncertainty estimations in this section are based.

This work's experimental portion involves modifying the dielectric layer on top of the photodiode. This mainly effects the absorption in the non-semiconducting part of the diode (section 2.2.2) and the surface recombination (section 2.2.7). It is important, however, to consider other factors to get an idea of the scope of uncertainty in the PQED structure.

2.2.1 Reflection

Starting at the front of the detector, the first barrier a photon meets is the surface. Some fraction of incident photons will be reflected off the front of the detector. This also applies to any material interfaces within the device where there is a change in the refractive index. The reflectance can be calculated based on refractive indices and the thickness of the passivation layers.

Two detector structures have been proposed for the PQED to minimize losses to reflection. The first is a phototrap consisting of two photodiodes placed at an angle to one another, creating several reflections of the incident beam, as shown in Fig. 2.2 [39]. This structure has been shown to have a reflectance loss of less than 1 ppm for specular reflections of p-polarized light [38], assuming less than 1 ppm diffuse reflection. For unpolarized light, the two-detector trap has been shown to have an uncertainty due to reflectance loss of less than 20 ppm over the applicable wavelength range [37].

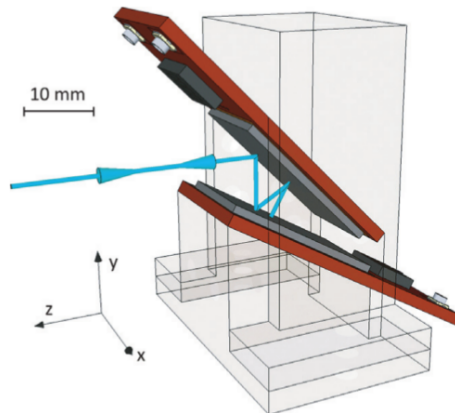


Figure 2.2: Schematic of the trap detector structure designed during the *qu-Candela* project.

If diffuse reflections prove to be a non-negligible loss, the photodiode may be placed inside a spherical mirror structure. Such a structure ensures the collection of all incoming photons [38]. Reflectance losses are thus principally accounted for and will be considered negligible elsewhere in this work.

2.2.2 Absorption

Photons absorbed outside the semiconducting areas of the photodiode will not contribute to the photocurrent. Absorption in dust particles on the surface of the detector and dielectric coatings on the front of the detector are the primary sources of this type of loss. According to Geist [14], cleanroom culture can limit the quantum deficiency due to absorption by dust particles to < 1 ppm.

In the SiO_x coating used in the original PQED detector, the quantum deficiency related to absorption in the film is predicted to < 0.001 ppm, assuming a $1 \mu\text{m}$ thick passivation layer [14]. This number is based on the typical transmission losses in a fiber optic cable

[14]. The original PQED was tested with two different oxide thicknesses, nominally 220 and 300 nm [30]. The detector based on the 220 nm oxide produced marginally better results. As the experimental work in this thesis involves replacing SiO_x with SiN_x , the losses due to absorption may become more significant and are a factor to consider.

2.2.3 Transmission

The penetration of a photon into the bulk of the detector does not always equate with absorption in the material; a certain fraction of photons will be transmitted through the detector.

The absorption coefficient α is a material parameter that describes the attenuation of light as it propagates through a material. This coefficient is highly wavelength- and temperature-dependent. In general, high energy, short wavelength photons will be absorbed closer to the surface, while longer, lower energy wavelengths penetrate deeper into the material.

In one dimension, the absorption coefficient is related to the local intensity of light in the material by the equation:

$$\frac{dI(x)}{dx} = -\alpha I(x) \quad (2.4)$$

where I is the incident light intensity. By assuming that α only depends on the photon energy, the Beer-Lambert law applies, giving a solution to equation 2.4 in the form:

$$I(x) = I_0 e^{-\alpha x} \quad (2.5)$$

where I_0 is the initial incident light intensity. The absorption coefficient α is directly related to the imaginary part of the refractive index k of the material by:

$$\alpha = \frac{4\pi k}{\lambda} \quad (2.6)$$

The absorption coefficient at 300 K in silicon for a wide range of wavelengths is tabulated by Green[19]. Using equation 2.5 and the tabulated absorption coefficient, we may get an idea of the absorption in a 500 μm thick wafer. Figure 2.3 below shows the relative light intensity through a silicon wafer to 500 μm depth for wavelengths within the applicable range.

As all EHP have to cross the junction of the detector to be registered in the external circuit, it is relevant to consider where they are generated. For the shortest wavelengths, the relative intensity at $\lambda = 400\text{nm}$ is reduced to 1 ppm 2 μm in the bulk, so that essentially all EHP are generated within this range. For the longest wavelength, $\lambda = 800\mu\text{m}$, 1 ppm relative intensity is achieved 200 μm in the bulk.

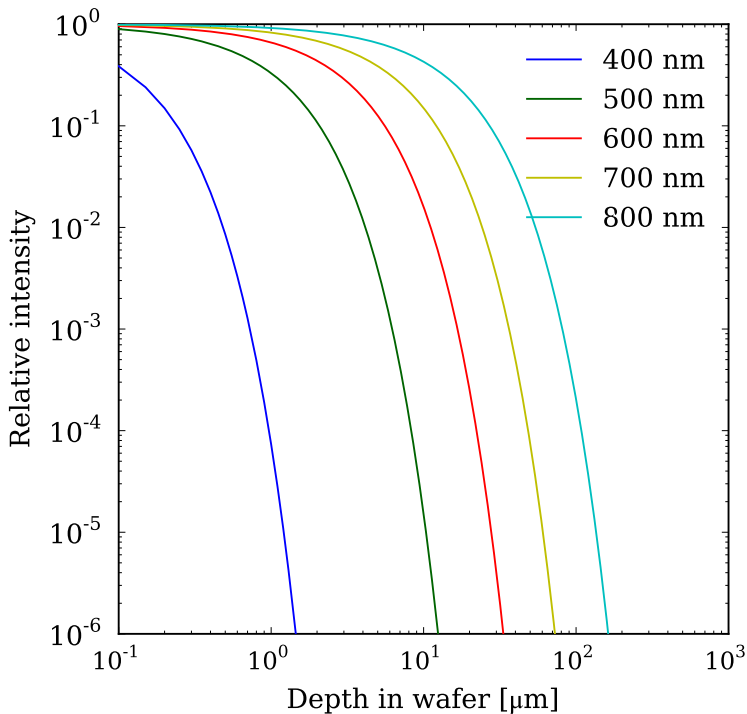


Figure 2.3: *The relative intensity of light through a silicon wafer at different wavelengths.*

In the applicable range of $\lambda = 400\text{--}800\text{nm}$, essentially all photon absorption is indirect. For photon energies larger than 3 eV, or $\lambda < 410\text{nm}$, direct optical transitions begin to occur [33]. The absorption exhibited by silicon is lower than that of a direct band gap semiconductor.

The absorption coefficient decreases with temperature [47]. The likelihood of transmission is thus increased as the temperature decreases, and more photons will be absorbed at shallower depths in the wafer. For this reason, the detector is predicted to have a higher quantum efficiency at low temperatures, and will be used at 77 K for the most accurate calibration purposes [18].

2.2.4 Free-Carrier Absorption

Some photons may be absorbed by a free carrier in the conduction band rather than promoting a carrier from the valence band. The free carrier will move higher into the conduction band and then relax back down to the top of the conduction band via *thermalization*, dissipating the energy gained from the photon in the form of phonons. Thermalization is an extremely fast process, so when free carrier absorption occurs the photon energy is inevitably lost. Based on cross-section data, Geist [14] predicts the quantum deficiency due to free-carrier absorption to be around 1 ppm.

Free-carrier absorption is most probable where there is the greatest concentration of free carriers. In the induced diode structure, this is in the induced depletion region near the surface of the substrate. It might be necessary to adjust the quantum deficiency loss in this area if the surface charge is increased, as this will increase the number of free carriers in the inversion layer.

2.2.5 Generation Current

The generation or dark current is a small current due to the random excitation of carriers across the band gap by thermal excitation. The uncertainty of this factor can be controlled by measuring the current before any light is applied, and then subtracting the contribution in order to correct for it. The generation current decreases with temperature.

This factor contributes negatively to the quantum deficiency; that is, it is a gain. Geist [14] estimates that the reverse bias dark current can be limited to less than -0.001 ppm at low temperatures, based on simulations in PC1D. The photogenerated current measured during PQED operation is 100 μA or smaller, while the dark current is the nA - pA range, but strongly bias dependent.

2.2.6 Bulk Recombination

Any photoexcited EHP not yet spatially separated by the junction may recombine by one of three mechanisms. Each mechanism has a characteristic lifetime τ , which is the average amount of time a minority carrier diffuses through the bulk before it recombines.

All EHP generated outside the depletion region must diffuse to this region in order to be separated. Depending upon the quality of the bulk material and the materials at the surfaces on either side of the detector, recombination can be a significant factor in the internal quantum deficiency (IQD). A long recombination lifetime increases the time the EHP diffuses before it recombines, and is generally desirable to this end.

The *injection level* Δn is the number of excess charge carriers in the material. We commonly distinguish between strong and weak injection levels. The thresholds for these are given by comparing the injection level to the majority carrier concentration. If the number of excess carriers is much less than the majority carrier concentration ($\Delta n \ll N_a$) we are operating in a weak injection regime. Conversely, the strong injection regime is when the injection level is much greater than the doping concentration. The working injection level range of PQED is on the order of $\Delta n = 10^{10} - 10^{12} \text{cm}^{-3}$.

The recombination lifetime for a certain mechanism is defined as the constant of proportionality between the recombination rate via that mechanism U and the injection level Δn :

$$U = \frac{\Delta n}{\tau} \quad (2.7)$$

The dependency between the recombination rate and the injection level is a complex relationship. Lifetimes are *injection-level dependent*. Equation 2.7 is therefore often non-linear.

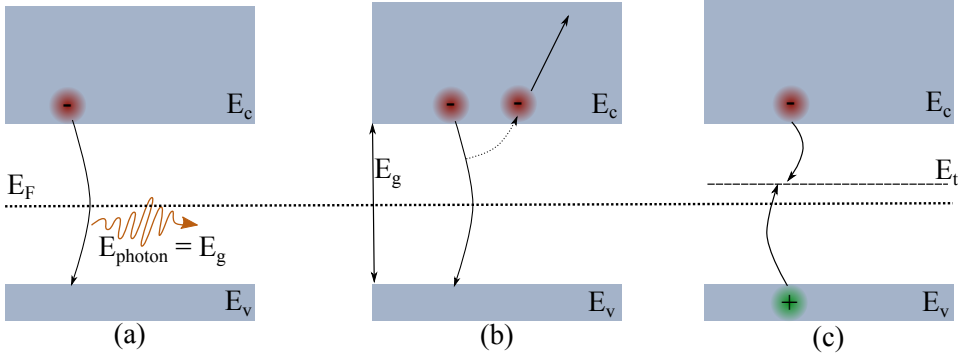


Figure 2.4: Recombination mechanisms, from left to right: radiative, Auger and SRH.

In *radiative recombination* (depicted on the left of Fig. 2.4), the electron recombines directly with a hole in the valence band by releasing a photon with energy corresponding to the band gap. In direct band gap semiconductors such as gallium arsenide, direct recombination is the most probable way for EHPs to recombine, and therefore generally has the shortest lifetime. In silicon, the indirect band gap decreases the probability of this transition.

In *Auger recombination* (depicted in the center in Fig. 2.4), an electron recombines with a hole by exciting a third charge carrier, either a hole further into the valence band or an electron higher into the conduction band. This third particle will quickly thermalize to the edge of the band gap. The probability of Auger recombination increases with Δn .

Impurity elements or dislocations in the crystal lattice form states in the forbidden band gap. *Shockley-Read-Hall (SRH) recombination* (depicted on the right in Fig. 2.4) is the recombination of EHPs via these forbidden states, called traps or recombination centers. The recombination centers captures electrons and holes, allowing them to recombine.

SRH recombination is highly dependent on the nature and density of the traps in the material. The best way to minimize such recombination is to use clean, monocrystalline materials with a minimum of impurities.

The bulk lifetime τ_{bulk} is given by the inverse sum of the lifetimes of all of the recombination mechanisms:

$$\frac{1}{\tau_{\text{bulk}}} = \frac{1}{\tau_{\text{auger}}} + \frac{1}{\tau_{\text{radiative}}} + \frac{1}{\tau_{\text{SRH}}} \quad (2.8)$$

The *diffusion length* $L_{n,p}$ is the average distance a minority carrier will travel before it recombines. The diffusion length of a minority carrier in a bulk semiconductor is:

$$L_{n,p} = \sqrt{D_{n,p}\tau_{\text{bulk}}} \quad (2.9)$$

where $D_{n,p}$ is the diffusion coefficient of the charge carrier. Ideally, the diffusion length of minority carriers in a detector should be on the order of the thickness of the device, so that an excited charge carrier will reach the depletion zone no matter where in the detector it is generated. However, a large depletion zone decreases this requirement as the charge carrier only needs to diffuse to the edge of this zone.

2.2.7 Surface Recombination

A surface is the abrupt termination of a crystal lattice, leaving unsaturated bonds that introduce energy states in the forbidden band gap. These states are called surface or interface states and are described by a density distribution $D_{it}(E)$ with the unit cm^{-2} . These states may act as traps in the same way as impurities in the bulk material. Recombination at a surface or interface may therefore be described using a formalism similar to SRH recombination in bulk. The main difference is that while SRH recombination describes a bulk (hence three-dimensional) property, surface recombination is a surface (and hence two-dimensional) property.

Tantamount to the general definition of a lifetime in bulk in equation 2.7, the *surface recombination velocity* (SRV) S of an interface may be defined by the following equation[4]:

$$U_s \equiv S\Delta n_s \quad (2.10)$$

where Δn_s is the excess minority carrier concentration at the surface. The SRV is so named because it is in units of velocity, as we are at a surface rather than in bulk and densities are in units of cm^{-2} rather than cm^{-3} .

The recombination rate via a single interface state at an energy E_t in the band gap is [4]:

$$U_s = \frac{v_{th} N_{st} (n_s p_s - n_i^2)}{\frac{n_s + n_1}{\sigma_p} + \frac{p_s + p_1}{\sigma_n}} = \frac{n_s p_s - n_i^2}{\frac{S_{p0}}{S_{p0}} + \frac{S_{n0}}{S_{n0}}} \quad (2.11)$$

where N_{st} is the number of surface states per unit area, $\sigma_{n,p}$ are the capture cross-sections of electrons and holes, respectively, and v_{th} is the thermal velocity of charge carriers. Furthermore n_s and p_s are the electron and hole concentrations at the surface and $n_1 \equiv n_i \exp\left(\frac{E_t - E_i}{kT}\right)$, $p_1 \equiv n_i \exp\left(\frac{E_i - E_t}{kT}\right)$.

S_{p0} and S_{n0} are the SRV parameters of electrons and holes, respectively, defined by $S_{n0} \equiv \sigma_n v_{th} N_{st}$ and $S_{p0} \equiv \sigma_p v_{th} N_{st}$.

A real surface contains a quasi-continuum of interface states. The recombination rate is then an integral over all of the surface states, as follows:

$$U_s = v_{th} \int_{E_v}^{E_c} \frac{D_{it}(E)(n_0 + p_0 + \Delta n_s)}{\frac{n_0 + n_1(E) + \Delta n_s}{\sigma_p(E)} + \frac{p_0 + p_1(E) + \Delta n_s}{\sigma_n(E)}} dE \quad (2.12)$$

where $D_{it}(E) \equiv \frac{dN_{st}}{dE}$ is the energy dependent surface state density. Note that the capture cross-sections $\sigma_{n,p}(E)$ are also energy dependent in this integral.

There are two main methods of limiting the SRV. The first, known as *chemical passivation*, is to decrease the density of interface states $D_{it}(E)$. This is generally accomplished by depositing a passivating thin film on the surface of the wafer under controlled, cleaned conditions.

The second method of limiting the SRV is to limit the concentration of either electrons or holes at the surface. As can be seen in equation 2.11, reducing the product $n_s p_s$ will reduce the recombination rate. This can be achieved by creating an electric field close to

the surface which repels one carrier type, for example by the presence of fixed charges. This method is known as *field-effect passivation*.

2.3 The Induced Diode

A native, positive fixed charge Q_f occurs in thermally grown SiO_x on silicon wafers. The charge is localized within a few nanometers of the interface, and the magnitude of the charge is determined by the growth temperature as well as the temperature of post-processing steps such as annealing [8]. The microscopic origin of this charge is discussed in chapter 2.4. The surface concentration of the fixed charge is practically limited to around $7 \times 10^{11} \text{cm}^{-2}$ in thermal silicon SiO_x on [111] silicon and several times lower for other crystallographic orientations [8].

When SiO_x is grown on a p-type wafer, the positive Q_f repels the positive holes in the wafer. The region near the SiO_x -Si interface will become depleted of holes and any free electrons will be drawn towards the interface. If there are enough positive charges at the surface of the oxide, an n-type inversion layer will form with a static electric field between the n and p-type region. We thus have the band bending required to form a rectifying junction, where the built-in potential between the inversion layer and the p-type bulk substrate acts as a charge separator. This structure is called an *induced diode*, because the n-type region is induced by the positive charges in the oxide. It was first described by Hansen in 1978 [20]. In recent years, this structure has emerged as a candidate for high quantum efficiency silicon photodiodes [18, 14].

Although SiO_x has been used thus far in the PQED, it can potentially be replaced by any dielectric with Q_f large enough to induce inversion. The positive charge intrinsically present in amorphous PECVD SiN_x is generally an order of magnitude larger than in SiO_x , which thus makes this a material of interest.

Figure 2.5 shows a schematic of the induced diode PQED design, taken from [39].

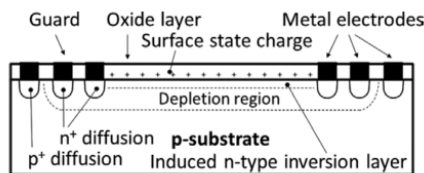


Figure 2.5: A cross-section of the original PQED induced diode design.

2.3.1 Band Structure

The band structure of an induced diode is the same as for a MOS capacitor under inversion conditions (see section 3.1.1 for a more complete discussion). A net positive charge in the dielectric causes the bands in the semiconductor to bend. If the Fermi level is drawn below the intrinsic Fermi level, inversion is achieved, resulting in the quasi n-p structure we call an induced diode.

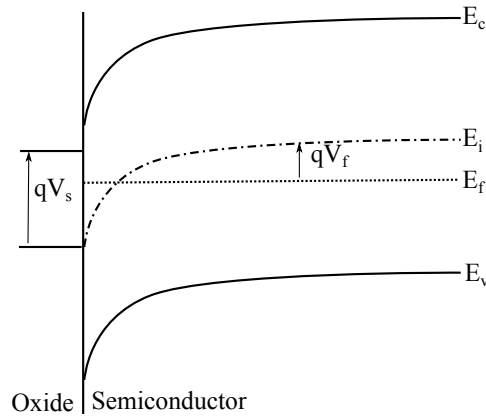


Figure 2.6: Band structure of an induced diode.

The state of strong inversion can be expressed as a condition on the surface potential:

$$\phi_s \geq 2\phi_F = 2 \frac{kT}{q} \ln \frac{N_a}{n_i} \quad (2.13)$$

This condition also implies that the concentration of electrons in the inversion region is equal to or greater than the concentration of holes in the bulk.

2.3.2 Charge Balance

Let us now consider a system as described above, with a layer of dielectric of arbitrary thickness x_0 on a p-type Si wafer with a doping concentration N_a . Figure 2.7 below shows a one-dimensional representation of the charge balance in the system, as described in [24]:

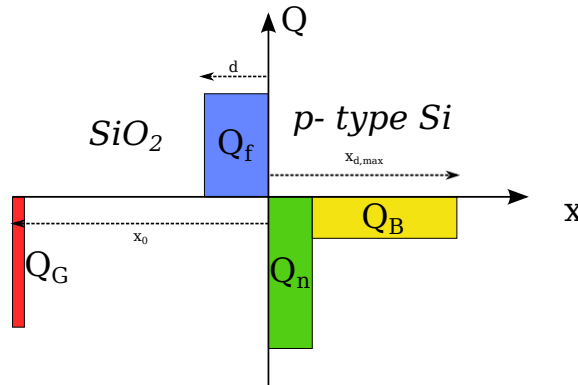


Figure 2.7: A one-dimensional model of the charge distribution in a self-induced diode.

where Q_f is the positive, fixed charge, Q_G is a mirror charge on the front of the dielectric, while Q_B is the negative depletion charge and Q_n is the inversion layer charge. The combined width of the depletion layer and inversion layer is denoted by $x_{d,max}$.

Figure 2.7 is a simplified picture of the charge distribution; the spatial charge variation is a continuum and does not drop off abruptly at the transition between the inversion and depletion regions. The rectangular geometry is a simple approximation which allows for the following derivation of Q_n .

By assuming total depletion of mobile charge carriers, and that the width of the inversion layer is negligible compared to the total depletion region width, the charges in the depletion layer are the dopant ions and the depletion charge can be expressed as [20]:

$$Q_B = -qN_a x_{d,\max} \quad (2.14)$$

Charge neutrality in the system requires all the charges in the system sum to zero:

$$Q_f + Q_n + Q_B + Q_G = 0 \quad (2.15)$$

We now assume a condition of strong inversion as in equation 2.13. We also assume that $d \ll x_0$, which is valid as the fixed charges in SiO_x are located within 2 nm of the SiO_x -Si interface [42]. By equating the potential drop across the structure to zero, the following equation is obtained [8]:

$$\frac{d\phi}{dx} = \frac{Q_G x_0}{\epsilon_{ox}} + \frac{Q_f d}{2\epsilon_{ox}} - \frac{Q_B x_{d,\max}}{2\epsilon_s} = 0 \quad (2.16)$$

where ϵ_{ox} and ϵ_s are the permittivities of the SiO_x and Si, respectively. By combining equations 2.15 and 2.16, the mirror charge Q_G can be eliminated. Q_n can then be expressed by the following equation [20]:

$$Q_n = -Q_f \left(1 - \frac{d}{2x_0}\right) - Q_B \left(1 + \frac{\epsilon_{ox} x_{d,\max}}{2\epsilon_s x_0}\right) \quad (2.17)$$

A portion of the fixed charge is compensated for by the mirror charge on the front of the oxide layer. The inversion charge decreases as a function of increasing mirror charge, while the mirror charge increases with decreasing SiO_x thickness. The SiO_x must therefore have a certain thickness in order to achieve inversion.

To maximize the collection efficiency of the detector, it is interesting to maximize the width of the depletion region. As in a MOS structure, the width of the depletion region is given by the equation:

$$W = \left[\frac{2\epsilon_s \phi_s}{qN_a} \right]^{\frac{1}{2}} \quad (2.18)$$

In the strong inversion state, the surface potential is given by equation 2.13 and equation 2.18 can be rewritten as:

$$W_{\max} = x_{d,\max} = 2 \left[\frac{\epsilon_s kT \ln(N_a/n_i)}{q^2 N_a} \right]^{\frac{1}{2}} \quad (2.19)$$

The size of $x_{d,\max}$ is maximized at the potential of strong inversion. Maximizing the size of $x_{d,\max}$ increases the collection efficiency of the diode, as all EHP generated in the depletion region are collected.

Figure 2.19 below shows the maximum width of the depletion region as a function of the doping concentration as in equation 2.19:

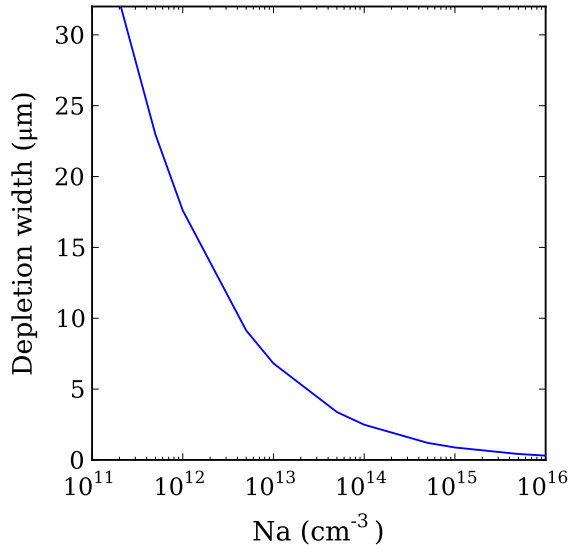


Figure 2.8: The depletion width W_{\max} as a function of the wafer doping N_a .

In the current Newstar project, diodes are being produced with doping conditions as low as $N_a = 0.7 \times 10^{12} \text{cm}^{-3}$. The width of the depletion region will thus realistically approach $20 \mu\text{m}$. Selecting a low doping concentration is advantageous as all EHP created in the depletion region are collected, so it should be as wide as possible for complete collection. Relating this to Fig. 2.3, we can see that with a depletion region of $20 \mu\text{m}$, all but 1 ppm of the incident photons at $\lambda < 500 \text{nm}$ are absorbed in the depletion region, while the fraction absorbed in the depletion region decreases exponentially with wavelength. Selecting the lowest doping concentration available is of interest when creating the PQED structure.

However, a low doped substrate also decreases the magnitude of band-bending, thereby retarding EHP separation. The diode will therefore be tested with several different doping concentrations in order to obtain the best solution.

2.3.3 Advantages of Induced Diodes

A silicon-based photodetector may be made in a number of ways, the most common of which is the pn-junction. The main advantages of using induced diodes in high efficiency photodetector structures are as follows:

High collection efficiency: For reasons discussed in section 2.3.2, high resistivity wafers are used in induced diodes. Doping impurities behave as recombination centers for SRH recombination. High resistivity wafers thus have a low defect density in bulk and therefore a longer bulk lifetime than corresponding low resistivity wafers.

Furthermore, no highly doped region is required to form the junction, as the n region is induced by the inversion layer. There are therefore no regions of high defect density, with the exception of the $\text{SiO}_x\text{-Si}$ interface, where there will always be a certain number of defects due to interface states. The recombination rate in the structure is thus potentially lower than a traditional pn-junction.

Complete collection of short wavelength photons [13]: The junction in the induced diode occurs in close proximity to the dielectric-silicon interface, and as demonstrated in section 2.3.2 extends up to 30 microns into the bulk. Short wavelength photons are absorbed close the $\text{SiO}_2\text{-Si}$ interface (as in Fig. 2.3), and are subject to a large electric field in this area. The EHP generated by these photons will essentially be entirely collected. By using lightly doped wafers, the depletion region can be extended relatively far into the bulk and the range of wavelengths for which complete collection occurs can be increased.

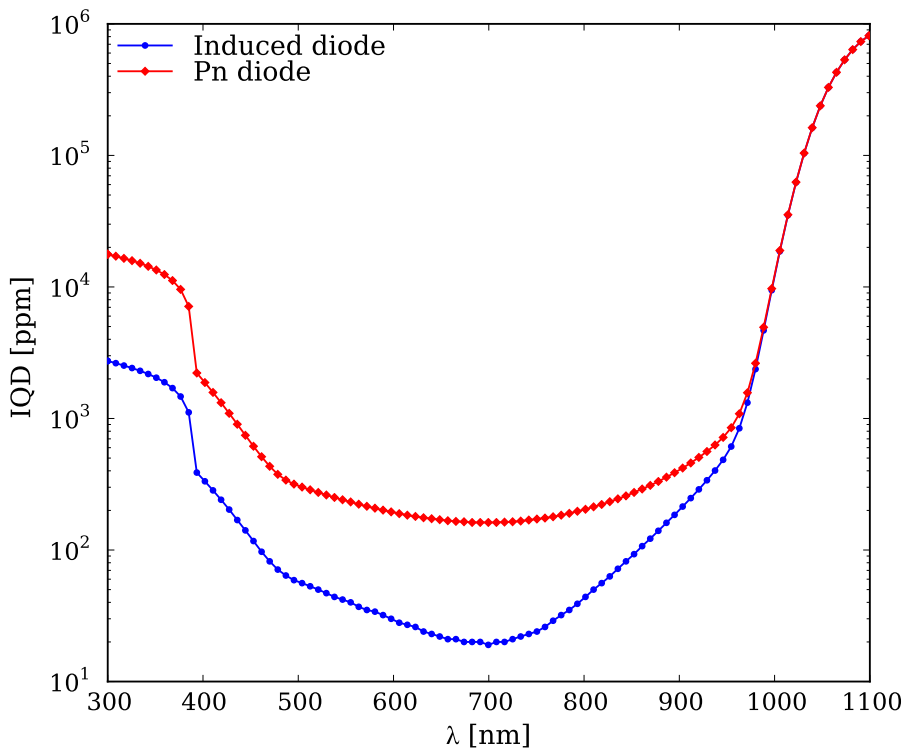


Figure 2.9: The internal quantum deficiency of a PN diode and an induced diode, as modelled in PC1D.

PC1D is a computer program commonly used for simulation of solar cells by simplified numerical solution of the semiconductor continuity equations and Poisson's equation. The program is not suited for complex analysis of the induced diode.

Among other things, the detector will be operated in reverse bias, which is not possible to simulate with PC1D. Nonetheless, PC1D simulations have been shown by Gran et al.[18] to correlate well with theoretical models for the diode. We have hence used the program to demonstrate the difference in quantum efficiency between a regular pn-junction and an induced diode, as shown in Fig. 2.9.

The simulations were performed on a 500 μm silicon wafer with a p-type doping density of $N_a = 4 \times 10^{12} \text{cm}^{-3}$. The device area was set to 2cm^{-2} , and the bulk lifetime to $\tau_{\text{bulk}} = 3.5 \text{ms}$. The surface recombination parameters $S_{p,n0}$ were set to 10^5cm s^{-1} , and an incident steady-state intensity of $100 \mu\text{W}$ was applied during the simulation. In the induced diode, $Q_f = 10^{12}$, while in the pn-junction, the n-type front diffusion was set to 10^{20}cm^{-3} . All of these parameters were selected to correspond to the experimental situation as closely as possible. We can thus see an order of magnitude difference in the IQD between the induced diode and the pn-junction modelled in Fig. 2.9.

Predictability: For the purposes of a primary standard, it is important that the diode be predictable. This means that all of the losses in the diode need to be quantified by a model, so that the correction terms in equation 2.3 can be determined accurately. In regular pn-junction diodes, diffusion processes are used to fabricate the n region. The junction is not abrupt, which makes the junction more difficult to model accurately. Alternatively one might epitaxially grow a pn-junction, which allows precise control but more complex processing. By comparison, the induced diode is a simple structure, composed of a single layer of dielectric on a high-resistivity Si wafer. As part of the Newstar project, detailed simulations are being made with the simulation software Genius [2] and Atlas [1] at Justervesenet and the University of Oslo, respectively, which will allow the correction factors for the responsivity to be determined accurately. It should be noted that Q_f also needs to be known or controlled precisely to ensure predictability.

Stability: The charges causing the inversion are *fixed*. The structure needs to stay invariant under successive light and bias cycles, and this is true of the fixed charges present in the silicon oxide currently used in the PQED structure.

2.3.4 Effects of Increasing the Fixed Charge

As indicated in the introduction, the principle goal of this thesis is to increase the fixed charge Q_f so as to improve performance of the induced photodiode. Although it has been made clear that increasing the fixed charge Q_f will increase the inversion charge, it is interesting to consider how this influences the quantum efficiency of the PQED.

Impact on the Surface Recombination Velocity

The electric field that exists in the semiconductor as a result of fixed charges in the dielectric attracts electrons towards the surface and repels holes. In addition to creating the aforementioned induced junction, this also effectively passivates the surface, and reduces the SRV.

This effect was simulated using extended Shockley-Read-Hall formalism as proposed by Girisch [16]. The system is solved using a program in Matlab following the algorithm as proposed by Aberle et al.[5]. The program was developed by Haug et al.[22]. Figure 2.10 below shows the variation of the surface recombination velocity with the fixed charge for several S_{p0} , the SRV parameter for holes. The SRV of holes is the relevant parameter in this case because there is a large concentration of electrons near the applicable surface, so that the SRV parameter for holes is the limiting factor in the recombination process.

The system simulated is 120 nm of SiN_x on Si with $N_a = 4 \times 10^{12} \text{cm}^{-3}$, at 300K with an injection level of $\Delta n = 10^{12}$. These parameters were chosen to correspond with the experimental conditions in this work as well as the actual operating conditions of the detector.

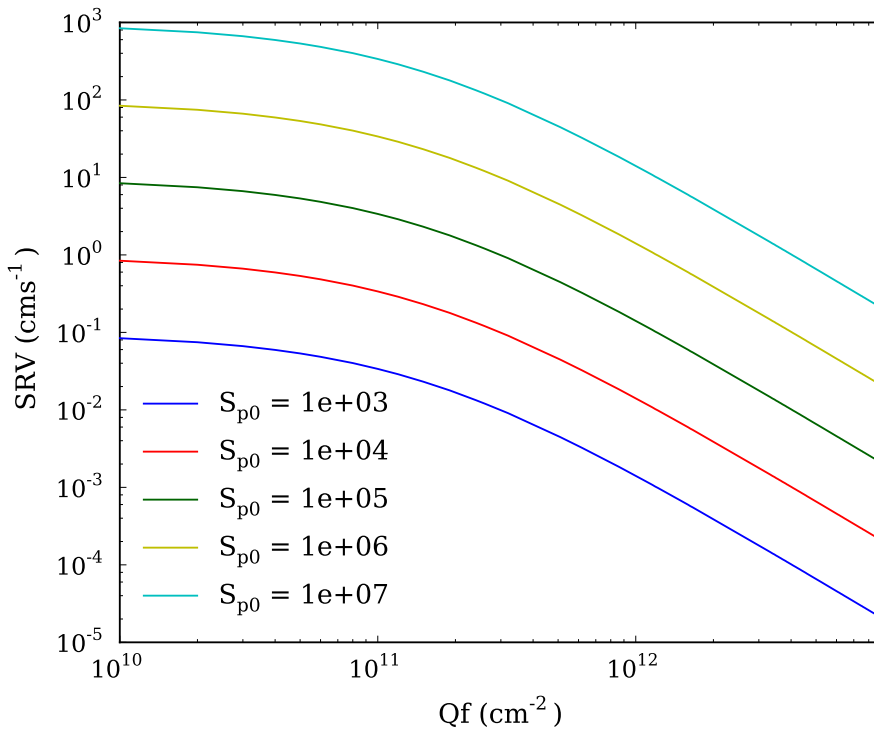


Figure 2.10: The surface recombination velocity at the SiN_x -Si interface as a function of the fixed charge.

The coefficient S_{p0} reflects the density of interface states and the capture cross-section of these states. A surface that is well-passivated chemically will have a small S_{p0} while the inverse is true of a badly passivated surface.

Next, one might inquire as to the correlation between the SRV and the quantum efficiency of the detector. Figure 2.11 shows the wavelength and fixed charge dependent internal quantum deficiency as a function of the SRV. These simulations were performed

using the modelling software Genius by Chi Kwong Tang at Justervesenet. The simulations are performed at 300 K, at a bias of -5 V, which reflect the actual operating conditions of the detector. The simulated induced diode has a p-type doping of $N_a = 2 \times 10^{12} \text{cm}^{-3}$, with a SRH lifetime of 400 μs .

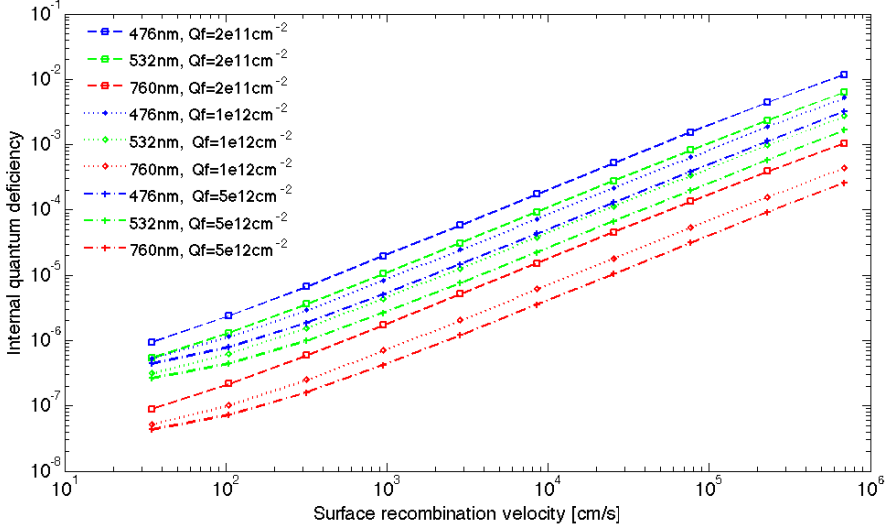


Figure 2.11: The IQD as a function of the SRV for several wavelengths and fixed charge densities.

As can be seen in Fig. 2.11, the IQD is predicted to decrease with SRV, so it is of interest to minimize it.

In order to achieve IQD on the order of 10 ppm, the SRV can be no more than 100 cm s^{-1} . Following the curves in Fig. 2.10 shows us that a combination of good chemical passivation (S_{p0}) and fixed charge is required in the dielectric to this end. The SRV begins to decrease strongly when Q_f is greater than 10^{12} .

Gran et al. [18]'s simulations of the PQED assumed $S = 10 - 100 \text{cm s}^{-1}$, so ideally at least this range should be achieved. The effective lifetime τ_{eff} of the original PQED was measured at a maximum of around 500 μm . Thus an increase in lifetime relative to this can be seen as an improvement.

Impact on the Quantum Efficiency at High Intensities

Increasing the fixed charge may also allow the PQED to function at high efficiencies at higher optical power. A greater flux of incoming photons will correlate directly to an increased injected charge Δn in the device. Therefore, increased optical power is simulated by varying the injected charge in Matlab simulations using the Girisch model as described above. Figure 2.12 shows the effect of the fixed charge on the SRV for different injection levels. Here we have taken $S_{p0} = 10^5 \text{cm s}^{-1}$.

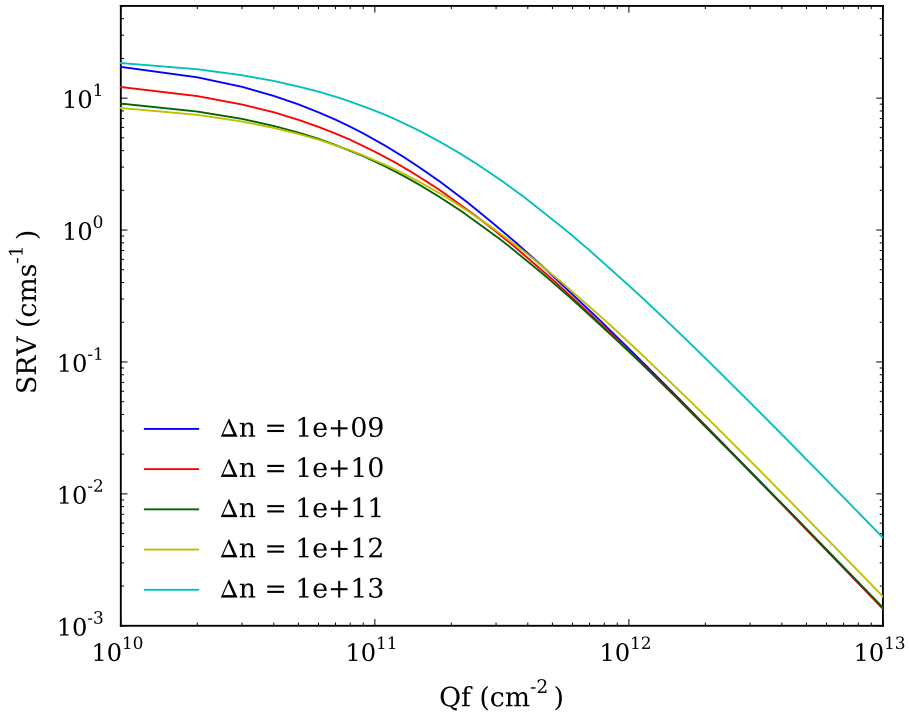


Figure 2.12: The SRV at the SiN_x -Si interface as a function of Q_f .

The SRV first decreases for increasing injection level before it increases for $\Delta n > 10^{11}$. Although the relative increase in SRV is the same at all Q_f levels, the absolute increase is much smaller for large Q_f . As was seen in Fig. 2.11, it is of interest to decrease the SRV as much as possible in order to maximize the QE.

2.4 Properties of Silicon Oxide and Silicon Nitride

Thus far, the induced diode has been discussed based on the assumption of an ideal insulator with fixed charges at the dielectric-Si interface. SiO_x has previously been the dielectric of choice for fabricating such as system. In this work, we consider the possibility of using SiN_x as a novel dielectric for an induced diode detector as it may allow a significant increase in Q_f . The two dielectrics will therefore be compared in terms of optical and electronic properties.

2.4.1 Silicon Oxide

Thermally grown silicon oxide (SiO_2) on silicon is one of the most commonly used materials in the electronics industry, and has thus been characterized extensively. The charges in SiO_2

were first characterized in 1967 [8]. Since then, the microscopic origin of these charges has been further explored. The charges found in SiO_2 are generally divided into four categories as follows [35]:

The interface trapped charge Q_{it} is the charge associated with the density of interface states D_{it} in the forbidden gap at the SiO_x -Si interface. The states may be positive or negative. These interface states may be annealed out [35].

The fixed oxide charge Q_f is a positive charge that occurs due to a silicon dangling bond defect with three oxygen back bonds (called P_{ox}). This charge density is localized within 2 nm of the SiO_x -Si interface [42]. These charges are constant and cannot be altered by illumination or applied voltage [4]. Q_f is determined by the oxidation parameters and the post-oxidation anneal [8].

The oxide trapped charge Q_{ot} is made up of electrons or holes trapped in bulk defects in the silicon oxide. These charges can also be reduced through low-temperature annealing processes.

The mobile oxide charge is due to ionic impurities such as Na^+ , Li^+ and K^+ . As the name suggests, these charges are mobile and thus undesirable in electronics applications as their movement disturbs the electrostatic balance of the system. These impurities can be reduced to negligible concentrations by clean processing as part of the SiO_x growth.

Since our goal is a *predictable* photodetector, we wish to employ a charge that is fixed in all cases. It is thus of interest to isolate the fixed charge Q_f in the PQED application. The magnitude of the fixed charge in silicon oxide is practically limited to $7 \times 10^{11} \text{cm}^{-2}$ [8].

SiO_2 can also provide excellent surface passivation, with $\text{SRV} < 10 \text{cm}^{-1}$ [9]. However, high growth temperatures and annealing are required to achieve the best passivation. These processes are antagonistic to the maximization of Q_f [8], which of course depends on the presence of defects.

Optical absorption in SiO_x starts at 8 eV [46], which means that it behaves as an almost ideal insulator over a wide spectral range and presents essentially no absorption in the visible range.

2.4.2 Silicon Nitride

Amorphous, nonstoichiometric, PECVD silicon nitride ($\text{SiN}_x\text{:H}$, commonly abbreviated to SiN_x) has become an important passivation material in the solar cell industry in the last several decades [9]. The ratios of Si, N and H in amorphous silicon nitride, and by extension, the electronic and optical properties, are highly dependent on the deposition parameters [12]. The optical band gap of SiN_x can be varied from 2 - 5.5 eV depending upon the ration of precursor gas flow [7]. In general, SiN_x becomes a less ideal insulator with decreasing stoichiometric nitrogen concentration x . The optical band gap should thus decrease with x .

The Si- SiN_x interface is less well understood than the Si- SiO_2 interface. The following discussion is based on Aberle's *Advanced Surface Passivation and Analysis* [4].

Like thermal SiO_2 , SiN_x contains a positive charge density. A very thin layer of SiO_2 occurs at the Si- SiN_x interface due to the exposure of the wafer to air between cleaning and deposition. The P_{ox} defect occurs in SiN_x films as well, creating a positive surface charge density of around 10^{11}cm^{-2} .

The dominant defect in SiN_x has been shown to be the Si dangling bond [11]. Furthermore, the silicon atom with the dangling bond is predominantly back-bonded to three nitrogen atoms. Such a configuration is called a *K-center*. K-centers are more stable in positive or negative configuration (K^+ and K^-) than in neutral configuration (K^0). The K-centers may emit electrons into the semiconductor, thereby becoming positively charged. These defects have been shown to extend ~ 20 nm into the bulk SiN_x [10]. Charged K-centers increases the fixed charge Q_f in SiN_x to $\sim 10^{12} \text{cm}^{-2}$.

Further more, K-centers may trap more holes upon the application of a negative gate bias, thereby increasing Q_f . However, the presence of electrons at the Si- SiN_x interface as is the case in the induced diode structure could possibly neutralize the K^+ centers over time.

Introduction to Characterization Methods

This chapter presents the theory of the key experimental methods used to perform the work on charging in nitride films.

In section 3.1, capacitance-voltage (CV) characterization is discussed. This technique allows the charges present in a dielectric to be quantified. The analysis of nitride CV curves can be complex, so it is important to understand a number of the artifacts that are present and how they may be interpreted.

In section 3.2, two important lifetime measurement techniques are discussed. Quasi-steady state photoconductance allows the determination of the effective charge carrier lifetime in a region of the wafer. Photoluminescence imaging creates an image of the lifetime across the whole wafer, and can thus be used to examine the uniformity of the lifetime.

3.1 Capacitance-Voltage Characterization

The capacitance-voltage (CV) characteristics of metal-insulator-semiconductor (MIS) capacitors can be used to analyze a number of characteristics of a given system, including the density of interface states D_{it} and the charge in the insulator. Due to the focus of this work on charged dielectrics, the theoretical discussion of MIS capacitors will concentrate on the characterization of the fixed charge. Material presenting this theory can be found in various books, but we have mostly relied on the works of Schröder [35] and Sze [43].

A capacitor is defined by its ability to store charge. We thus define capacitance as the change in stored charge Q due to a change in voltage V :

$$C = \frac{dQ}{dV} \quad (3.1)$$

For a parallel-plate capacitor containing an ideal insulator, the capacitance is given by

the equation:

$$C = \frac{\epsilon_r \epsilon_0 A}{d} \quad (3.2)$$

where ϵ_r is the relative permittivity of the insulator, ϵ_0 is the permittivity in vacuum, A is the surface area of the capacitor and d is the insulator thickness.

A MIS capacitor behaves like a series connection of the insulator and semiconductor capacitances. The insulator capacitance C_i is constant, and may be estimated by equation 3.2. Mobile charges in the semiconductor shift under applied voltage, so that the semiconductor capacitance C_s depends on the applied voltage. The total capacitance C_{tot} measured in the system is thus given by the equation:

$$C_{tot}(V) = \frac{C_i C_s(V)}{C_i + C_s(V)} \quad (3.3)$$

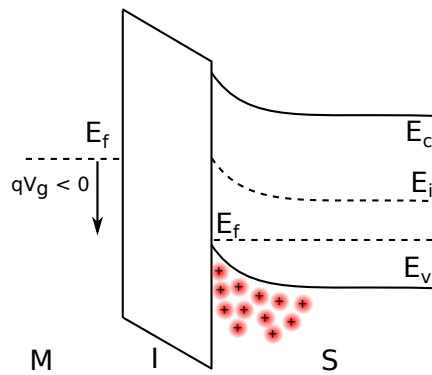
During a CV sweep, a range of DC gate voltages V_g are applied to the MIS structure. As can be seen in equation 3.1, the voltage must change for the capacitance to be measurable. A small-signal AC voltage is thus used to probe the capacitance at each DC voltage point, producing a CV curve. We will first consider the CV behavior of an ideal MIS structure before moving on to the non-ideal structures typically measured in this work.

3.1.1 Ideal MIS Capacitors

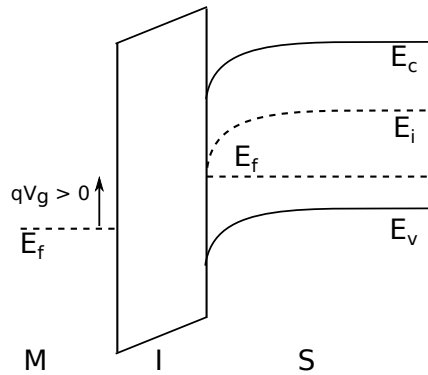
An ideal MIS structure is defined by the following assumptions [43]:

- No charges in the insulator.
- No carrier transport through the insulator (infinite resistivity).
- No difference between the metal and semiconductor work functions, so that there is no band-bending in the semiconductor in the absence of an external voltage.

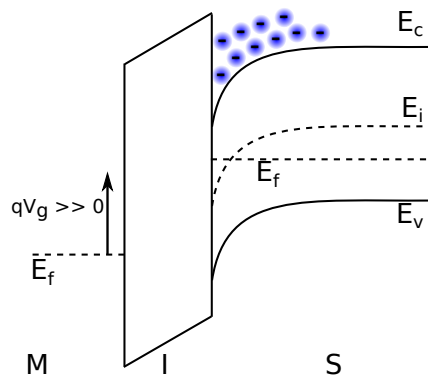
An applied voltage across the MIS will cause band-bending in the semiconductor. Since the insulator is assumed to be perfect, no current can pass through the system and the Fermi level must thus remain flat. The band-bending, however, will change the amount of charge stored near the insulator-semiconductor interface so that the capacitance of the system depends upon the applied DC voltage. Varying the DC voltage drives the system through three distinct states, with energy bands illustrated in Fig.3.1.



(a) A p-type MIS capacitor in accumulation.



(b) A p-type MIS capacitor in depletion.



(c) A p-type MIS capacitor in inversion.

Figure 3.1: Band diagrams of accumulation, depletion and inversion in an ideal p-type MIS capacitor.

Accumulation (Fig.3.1a) is the state of increased majority charge carrier concentration with respect to the bulk near the insulator-semiconductor interface. In a p-type semiconductor, this occurs when negative voltages are applied so that the bands bend upward. In accumulation, the capacitance of the semiconductor is large. Following equation 3.3, the total capacitance approaches the insulator capacitance C_i .

Depletion (Fig.3.1b) is the absence of mobile charges near the insulator-semiconductor interface. In a p-type semiconductor, this occurs when small, positive voltages are applied so that the bands bend slightly downward. The applied field thus drives majority charge carriers away from the interface. The capacitance of the semiconductor decreases, decreasing the total capacitance of the system. The size of the depletion region increases as a function of the gate voltage during depletion.

Inversion (Fig.3.1c) is the accumulation of minority carriers close to the insulator-semiconductor interface. In a p-type semiconductor, this occurs when large, positive voltages are applied so that the valence bands are bent strongly downward. The behavior of the total capacitance in this case will depend upon the small-signal AC frequency. At low frequency, the minority carriers will be able to follow the AC signal and the capacitance of the semiconductor will once again increase, maximizing the total capacitance towards C_i . At high frequency, the minority carriers are not able to follow the AC signal, and the semiconductor capacitance will remain small. At the point of inversion, the width of the depletion region has reached its maximum as described by equation 2.19.

CV sweeps are customarily performed from inversion to accumulation, and then in reverse. The sign of the voltage will depend on the doping polarity of the substrate. In this work, we operate exclusively with p-type substrates, so that all CV sweeps are performed from positive to negative gate voltages followed by the reverse. Sweeps from positive to negative gate voltages will be referred to as a *forward* sweep, while the opposite will be referred to as a *reverse* sweep.

The blue lines in Fig.3.2 below show a typical CV curve of an ideal MIS capacitor, passing through each of the conditions as discussed above:

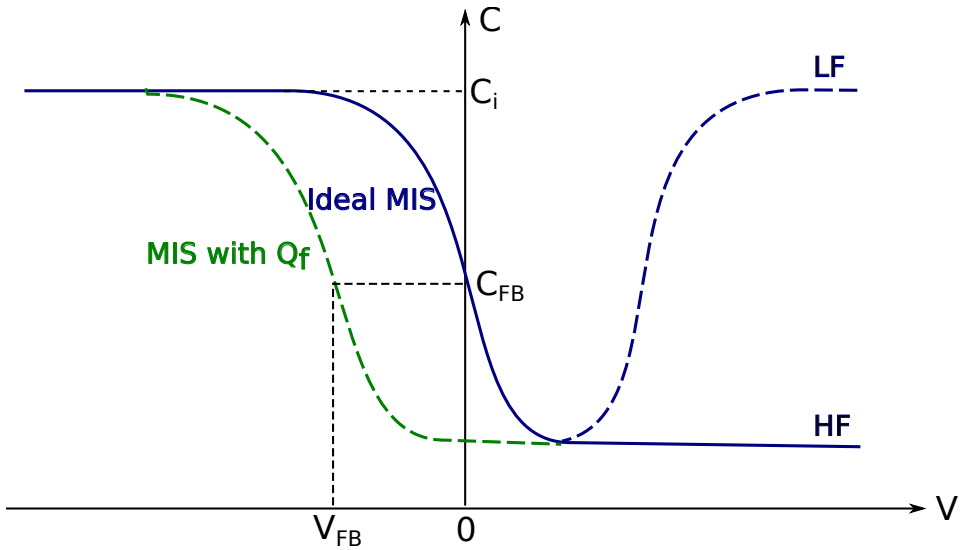


Figure 3.2: An ideal CV sweep of a MIS capacitor with no fixed charge, at low frequency and with a fixed charge Q_f .

The blue dashed line in Fig.3.2 shows the behavior of a CV curve when low AC probe frequencies are applied to the system, while the solid blue line show the behavior at high AC probe frequencies. The green line shows a system containing fixed charges, which will be discussed in detail in the following section.

Between the accumulation and depletion conditions, the system passes through a flatband voltage V_{FB} (see Fig.3.2), the point at which there is no band-bending in the semiconductor. In an ideal MIS capacitor, the bands are flat at 0 V. In the section 3.1.2 below, we see how non-ideal insulator behavior can shift the flatband voltage.

3.1.2 Real MIS Capacitors

A number of factors cause CV sweeps to deviate from the ideal case. The following section details the main mechanisms applicable in interpreting CV curves in this work.

Work Function Difference

First of all, there is a work function difference between the metal and the semiconductor, which can be expressed by the following equation:

$$\Delta\phi_{ms} = \phi_m - \chi - \frac{E_g}{2q} - \frac{kT}{q} \ln\left(\frac{N_a}{n_i}\right) \quad (3.4)$$

where ϕ_m is the metal work function, χ is the electron affinity of the semiconductor, E_g the semiconductor band gap, N_a the doping concentration, and n_i the intrinsic carrier concentration. The work function for aluminium, the metal used in this work, is $\phi_m = 4.1\text{eV}$ as measured by CV [45]. By inserting applicable values for silicon as the semiconductor,

and taking a doping concentration of $N_a = 4 \times 10^{12} \text{cm}^{-3}$, which is applicable for this work, the work function difference is $\Delta\phi_{\text{ms}} = -0.11 \text{eV}$.

Fixed Charges

As discussed in section 2.4, insulators such as SiO_x and SiN_x may contain fixed charges near their interface with silicon. This fixed charge has the same effect as an applied voltage: it causes band-bending in the semiconductor. The presence of band-bending at 0 V causes a horizontal shift in the ideal CV curve (as depicted by the green line in Fig.3.2). The charge present in the insulator may be determined by means of extracting the flatband voltage from a CV curve.

At the flatband voltage V_{FB} , the semiconductor capacitance can be estimated using the Debye length L_D , which describes charge screening in the semiconductor. The semiconductor capacitance at flatband voltage is thus given by the following equations:

$$L_D = \sqrt{\frac{\epsilon_{\text{Si}} kT}{q^2 N_a}} \quad (3.5a)$$

$$C_s(V_{\text{FB}}) = \frac{\epsilon_{\text{Si}} \epsilon_0 A}{L_D} \quad (3.5b)$$

The constant insulator capacitance C_i can be found either using equation 3.2 or extracted from the CV curve. The total flatband capacitance $C_{\text{tot}}(V_{\text{FB}})$ can then be calculated using equation 3.3, and the flatband voltage can then be extracted from the CV curve.

By assuming that all charges in the insulator are fixed, the charge density in the insulator is then determined using the following equation:

$$Q_f = \frac{C_i}{Aq} \left(\Delta\phi_{\text{ms}} - V_{\text{FB}} \right) \quad (3.6)$$

For simplicity, the notation Q_f will henceforth be used to refer to *all* charges stored in the insulator, as opposed to only the fixed charges. This is partially due to the difficulties of differentiating between different types of charge in SiN_x films.

Hysteresis

Equation 3.6 in the previous section assumes that any charge present in the insulator is fixed. In reality, neither SiO_x nor SiN_x are perfect insulators, and charges may pass between the silicon and the dielectric. Charges may be stored in defect states D_{it} near the interface. This effect causes hysteresis in the CV sweeps, which presents itself as a horizontal shift in the reverse sweep relative to the forward sweep. Essentially, this means that the gate voltage applied during the sweep has charged some of the defect states, so that the charge Q_f has effectively changed during the sweep. For detector applications, we generally wish to know the charge that was present previous to the sweep, as no gate voltage is applied during detector operation. As the first forward sweep gives the value of Q_f that has least been affected by the gate biasing, this value is taken to be correct.

Series Resistance

In this work, the wafers used to fabricate MIS capacitors have a very high resistivity so as to maximize the width of depletion zone and hence the collection region in the detector. There is a substantial series resistance in the measurement circuit due to the resistance of the bulk wafer itself. Figure 3.3 shows a circuit diagram of a MIS capacitor including the series resistance due to the bulk.

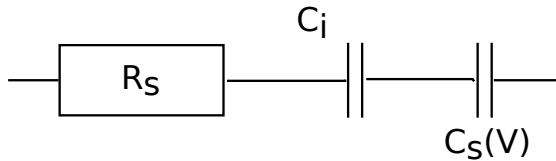


Figure 3.3: Circuit diagram of a MIS capacitor with series resistance.

The series resistance retards the charging of the capacitor in a manner analogous to an RC filter. This manifests as a decreased measured capacitance during CV sweeps, the effect of which increases with frequency. The C_i level as shown in Fig.3.2 essentially becomes frequency-dependent. The effects of series resistance can be identified by comparing the magnitude of the C_i value in the CV sweep to the theoretical value; if they are of a similar order of magnitude we assume the effects of the series resistance to be negligible.

Leakage Current

Defects in the insulator may allow current to leak through it. A typical defect that allows the passage of current is a pinhole defect, which occurs when the film is not completely dense, so that there are tiny holes in the film. Upon the application of high biases, pinholes may cause fatal dielectric breakdown.

More minor leakages via other impurities in the film are also possible. These typically cause the C_i level shown in Fig.3.2 to slant downwards. Although leakage current does not affect the operation of the induced diode, it ruins many CV measurements.

3.2 Measuring Lifetime

All types of lifetime measurements yield the effective lifetime τ_{eff} of minority charge carriers in a sample. The effective lifetime in a slab semiconductor reflects both the bulk and surface properties of the sample, and can generally be expressed by the following equation [36]:

$$\frac{1}{\tau_{\text{eff}}} = \frac{1}{\tau_{\text{bulk}}} + \frac{1}{\tau_{\text{surface}}} \quad (3.7)$$

The shortest lifetime will dominate the effective lifetime. Depending on the relative sizes of the lifetimes in bulk and at the surface, equation 3.7 can be rewritten. If the surface is bad, i.e. the τ_{surface} is short, the total recombination is diffusion limited. This means that the limiting factor in the lifetime is how fast charge carriers diffuse to a surface to recombine. τ_{eff} can then be expressed by the equation [4]:

$$\frac{1}{\tau_{\text{eff}}} = \frac{1}{\tau_{\text{bulk}}} + \left(\frac{\pi}{W}\right)^2 D_{n,p} \quad (3.8)$$

where W is the width of the wafer and $D_{n,p}$ is the diffusion coefficient of minority carriers. If the opposite case is true, and the SRV is small, τ_{eff} is independent of minority carrier diffusion. τ_{eff} can then be expressed by the equation:

$$\frac{1}{\tau_{\text{eff}}} = \frac{1}{\tau_{\text{bulk}}} + \frac{2S_{\text{eff}}}{W} \quad (3.9)$$

The following sections theoretically describe two methods used to quantify τ_{eff} .

3.2.1 Quasi-Steady State and Quasi-Transient Lifetime Measurements

By illuminating a sample with a light pulse and measuring the change in conductance, τ_{eff} may be determined in one of two ways, *quasi-transient* or *quasi-steady-state* photoconductance (QSSPC) measurements. Both involve a simplified solution of the continuity equation for excess charge carrier density in a semiconductor, given by the following equation [31]:

$$\frac{\delta \Delta n}{\delta t} = G - U + \frac{1}{q} \nabla J \quad (3.10)$$

As the semiconductor is illuminated with a spatial large light pulse, uniform photogeneration is assumed so that the last term in equation 3.10 is set to zero. Applying equation 2.7, equation 3.10 may be rearranged as:

$$\tau_{\text{eff}}(\Delta n) = \frac{\Delta n(t)}{G(t) - \frac{\delta \Delta n}{\delta t}} \quad (3.11)$$

The excess carrier concentration increases the wafer conductance as expressed by the following equation [40]:

$$\sigma = q \Delta n (\mu_n + \mu_p) W \quad (3.12)$$

where W is the wafer thickness, and $\mu_{n,p}$ are the mobilities of electrons and holes, respectively. The conductance in an area of may be measured using inductive coils, and hence Δn determined. Furthermore, the generation rate G may be calculated based on the intensity of the light and the reflectance of the sample.

With the excess carrier concentration and generation rates known, equation 3.11 may be simplified depending on the character of the incident light pulse. In *transient photoconductance* measurements, the pulse is much shorter than the decay time of the charge carriers. Hence $G(t) \ll \delta\Delta n/\delta t$, and equation 3.11 simplifies to:

$$\tau_{\text{eff}}(\Delta n) = \frac{\Delta n(t)}{\frac{\delta\Delta n}{\delta t}} \quad (3.13)$$

For a long pulse, the inverse is true and $G(t) \gg \delta\Delta n/\delta t$. We are then under the conditions *quasi-steady-state photoconductance*, where the decay time of the light pulse is so slow that the system is assumed to be in steady-state. Equation 3.11 simplifies to:

$$\tau_{\text{eff}}(\Delta n) = \frac{\Delta n(t)}{G(t)} \quad (3.14)$$

By changing the length of the light pulse, quasi-transient and quasi-steady state measurements may be made using the same set-up. Both methods involve a simplified solution of equation 3.11, and thus both have their limitations. The quasi-transient solution works best on samples with relatively long lifetimes, as the lifetime must be significantly longer than the applied light pulse.

The resolution of a photoconductance measurement is limited by the size of the inductive coil used to measure the conductance, generally a few centimeters in diameter. The measurement yields the lifetime at the point of measurement, which may or may not be representative for the entire sample.

3.2.2 Photoluminescence Imaging

Photoluminescence (PL) imaging creates a lifetime picture of a sample, which allows for a look at the spatial variation of τ_{eff} . EHP in an illuminated sample may recombine radiatively, as discussed in section 2.2.6. In PL imaging, a laser is used to illuminate a large area, and a camera registers the luminescent light resulting from radiative recombination [44].

Each pixel in a PL image initially represents a number of photon counts in the time used to take the image, which of course is an arbitrary number as it depends on the length, wavelength and intensity of the incident pulse. PL images may be calibrated using an integrated QSSPC setup [23], yielding a map of τ_{eff} across the sample. The injection level may be varied by varying the intensity of the incident light.

PL images only take a few seconds to acquire, and their spatial resolution is limited by the pixel size of the camera. Figure 3.4 shows a PL set-up with an integrated QSSPC coil, taken from [21].

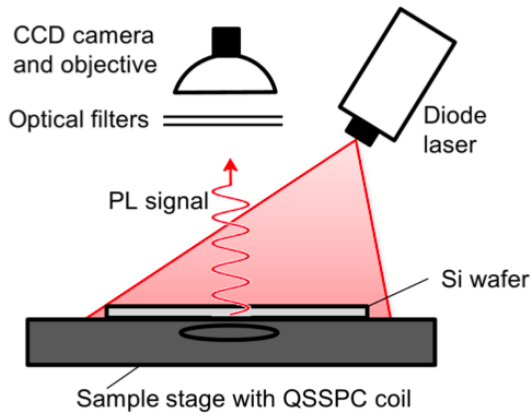


Figure 3.4: A general schematic showing a PL set-up.

Experimental Methods

4.1 Sample Fabrication

All of the samples were fabricated using wafers from a single batch. The general characteristics of the wafers are summarized in Table 4.1.

Manufacturer	Okmetic
Growth method	Czochralski
Doping	p-type
Thickness	500 μm
Diameter	4 inch
Crystal orientation	[111]
Average resistivity	3300 Ωcm
Average N_a	$4 \times 10^{12}\text{cm}^{-3}$

Table 4.1: Characteristics of the wafers.

The crystallographic orientation [111] was selected in the early stages of this work because it provides the maximum fixed charge Q_f when growing thermal SiO_x [8]. Since this work does not deal with thermal SiO_x , the orientation is less relevant.

The wafers were dipped in hydrofluoric acid to remove the surface oxide layer that is formed on any wafer exposed to air, and then rinsed in deionized water before deposition to remove the native silicon oxide at the wafer surface before deposition was performed.

4.1.1 Plasma-Enhanced Chemical Vapor Deposition (PECVD)

Chemical vapor deposition is a method used to deposit thin films by reacting gaseous precursors over the surface of the substrate. In plasma-enhanced chemical vapour deposition (PECVD), a plasma is used to increase the reaction rate of the precursors, allowing the processing temperatures to be kept low. PECVD has been used to deposit silicon nitride

(SiN_x:H) and amorphous silicon (a-Si) on the aforementioned p-type wafers to explore the interface and fixed charges in nitride films as well as the surface recombination velocities.

The PECVD reactor used in this work was a PlasmaLab 133 system from Oxford Instruments installed in the IFE Solar Cell Laboratory. A high RF frequency of 13.56 MHz is used to generate the plasma.

Two different SiN_x compositions were used. Table 4.2 below summarizes the PECVD deposition parameters of the nitrides as well as a-Si.

Parameter	Type 1 SiN _x :H	Type 2 SiN _x :H	a-Si:H
Temperature [° C]	400	400	200
Power density [mW/cm ²]	46.8	46.8	46.8
Chamber pressure [mTorr]	800	800	300
SiH ₄ flow [sccm]	20	10	25
NH ₃ flow [sccm]	20	20	0
N ₂ flow [sccm]	980	980	0
N ₂ O flow [sccm]	0	0	0
TMA ¹ flow [sccm]	0	0	0

Table 4.2: PECVD deposition parameters for the two types of nitride film deposited in the sample set.

Although the exact chemical composition of the films was not determined, it may be noted that decreasing the silane (SiH₄) flow in the reactor effectively decreases the fraction of silicon in the films, or increases the x in SiN_x. This is known to change the electronic and optical properties of the SiN_x [12, 27].

Table 4.3 summarizes the samples fabricated, including the thicknesses and refractive indexes predicted based on knowledge of the reactor. The actual measured thickness and refractive indexes are presented in section 5.1.1.

Sample	Film type	Deposition time	Nominal thickness	Nominal refractive index at $\lambda = 600\text{nm}$	Wafer types
1	Type 1	8 min 40s	120 nm	2.04	Lifetime and CV
2	Type 2	9 min 20s	120 nm	1.88	Lifetime, CV and CV/PI
3	Type 2	6 min 13s	80 nm	1.88	Lifetime, CV
Reference	a-Si	5 min	-	-	Lifetime reference

Table 4.3: The characteristics of the sample set.

Several wafers were made of each of the samples, as indicated in the last column of Table 4.3. The wafers types are described as follows:

Lifetime wafers were deposited with a-Si for 5 minutes on the backside in addition to

nitride on the front side.

CV wafers were further metallized as described in section 4.1.2.

PL/CV wafers were deposited with a-Si for 5 minutes on the reverse side, and were further metallized as described in section 4.1.2. This type was only made with sample 2, as it was shown to have the best characteristics for the applications in this work.

The lifetime reference wafer had a-Si on both sides, and was annealed for 10 minutes at 450 °C in a belt furnace to further improve the passivation. This sample was used to calibrate the bulk lifetime of the wafer set.

A circular ring of defects was visible on the a-Si side of samples 1, 2 and 3, extending approximately 1 cm towards the center of the wafer on all sides. It was concluded that this was a problem of adhesion in the wafer edge. Since the lifetime in these areas was extremely poor, the outer areas of the wafer were not used. Figure 4.1 below shows the defects observed in the a-Si.

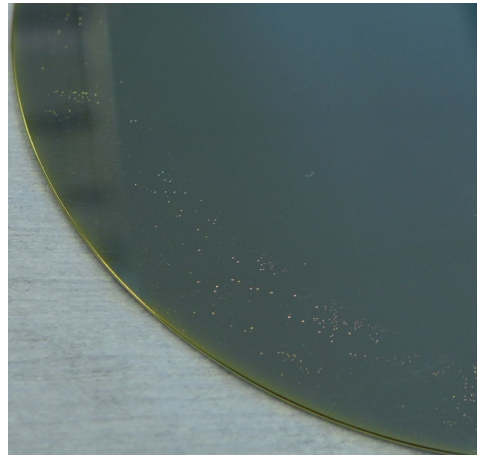


Figure 4.1: *The defects seen in the a-Si deposited on all of the wafers.*

4.1.2 Electrode Metallization

A Kurt J. Lesker Company NANO 36 thermal evaporation system was used to deposit aluminum electrodes on the front and back sides of the wafers. In thermal evaporation, the metal of choice is evaporated by running a large current through a crucible containing small pellets of the metal. The sample is mounted above the crucible in a vacuum chamber. A shadow mask is used to define the electrode areas. Use-specific shadow masks were created by cutting the desired electrode pattern into another silicon wafer with a Rofin laser. The evaporated metal is thus deposited through the shadow mask onto the substrate. The sample mount rotates so as to ensure even coverage.

In order to perform CV measurements, CV and CV/PL wafers needed front and backside electrodes, to form MIS structures. The CV wafers were deposited with approximately

150 nm of aluminum on the entire backside. The backside electrode of the CV/PL wafers was a ring around the edge of the wafer, so as to keep the a-Si for good lifetime during PL characterization. The wafers were then annealed for 5 minutes at 450 °C. This heat treatment allows a eutectic phase to form at the silicon-aluminum interface, thereby creating an alloy which improves quality of the electrode.

The front (SiN_x) side electrodes were circular electrodes deposited in a grid formation. The electrode diameter was 2 mm on the CV wafers and 8 mm on the CV/PL wafers. Figure 4.2 below shows photos of the front side of each sample. An area of the CV/PL was left empty to provide a space for performing QSSPC calibrations of the PL images.

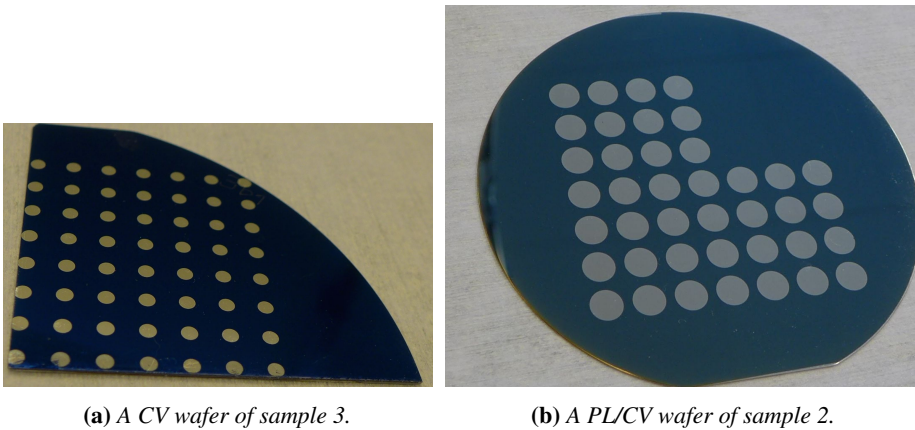


Figure 4.2: Images of the two sample types.

4.2 Characterization

4.2.1 Ellipsometry

Ellipsometry was used to determine the thickness and refractive index of the SiN_x films. The results were further analyzed to determine the absorption in the films, and hence their suitability for photodetector applications.

A variable angle spectroscopic ellipsometer (VASE) from J. A. Woollam Co., Inc. was used to perform the ellipsometric measurements in this work. Polarized, monochromatic light is reflected from the sample surface and the change in polarization is measured with a detector.

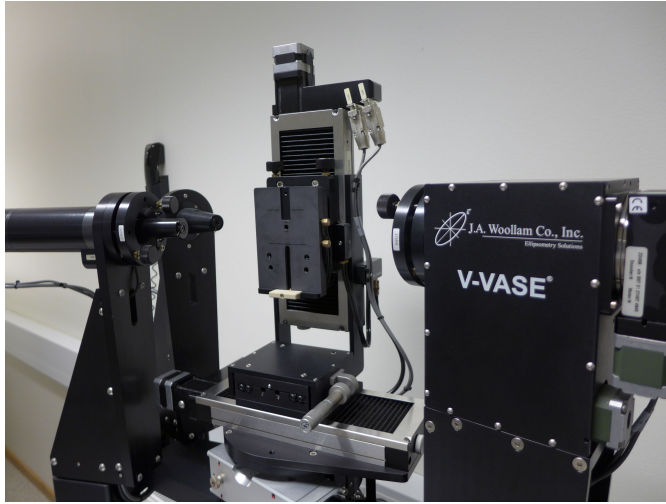


Figure 4.3: The J.A. Woollam variable angle spectroscopic ellipsometer.

The polarization of light is described by two components: the s-polarization and p-polarization. P-polarized waves are parallel to the plane of incidence while s-polarized waves are perpendicular. Using linear polarized light, the amplitude ratio of the reflected beam ψ and the phase shift Δ are measured. These quantities are related to the normalized amplitudes of the two beam components R_s and R_p by the equation:

$$\frac{R_p}{R_s} = \tan(\psi) \exp(i\Delta) \quad (4.1)$$

The spectroscopic parameters ψ and Δ are measured as a function of wavelength. These can be fitted to models of varying complexity in order to determine the thickness, refractive index and absorption in the films.

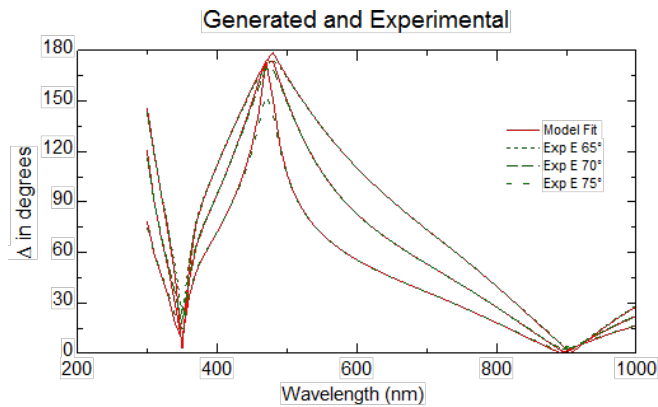


Figure 4.4: The ellipsometric fit for Δ of sample 1.

4.2.2 Photoluminescence Imaging

Photoluminescence (PL) images were collected using a BT imaging LIS-R1 setup with an integrated Sinton QSSPC stage. The control voltage of the laser was kept constant at 2.2 V. This corresponded to an injection level of approximately $\Delta n = 3 \times 10^{14} \text{cm}^{-2}$. All PL images were taken with the a-Si passivated side facing up, and the reflectance this surface was assumed to be 30 %. As this is several orders of magnitude higher than the intended use level of the detector, the absolute value of the lifetimes may not be entirely correct.

Unfortunately, the QSSPC curves produced by the Sinton stage in the PL set-up produced data that were clearly fallacious. The PL images were therefore calibrated using external QSSPC data in Matlab. Post-calibration involved correlating the pixels in a certain area of the image to a lifetime value from a QSSPC file. For this to be accurate, the QSSPC data needed to be correlated to the same area on the wafer where the image was taken. Correctly aligning the QSSPC coil in the same place in the two separate set-ups proved to be non-trivial, and this may have produced some errors in the calibrated data.

4.2.3 Quasi Steady-State Photoconductance Decay

QSSPC measurements may be interpreted by either assuming transient or steady-state conditions, as described in section 3.2.1. In practice, both transient and steady-state measurements were conducted by changing the flash length from its longest setting (1/1) for steady-state measurements to its shortest setting (1/64) for transient measurements, and then changing the analysis type in the Sinton spreadsheet. Both measurements were performed to get an idea of the uncertainty related to the measured lifetime.

4.2.4 Capacitance-Voltage Set-up

Capacitance-voltage characterization and experiments charging the films were performed using a Keithley 4200-SCS semiconductor characterization system with a Signatone S-1060 QuieTemp Hot Chuck sample mount.

All work was performed in CVU voltage sweep mode. Presoak voltage and hold time, start and stop voltages of the sweep, voltage step size, the delay between subsequent measurement points, and the AC frequency and amplitude can all be adjusted. The Keithley set-up provides DC voltages up to $\pm 30 \text{V}$, and AC frequencies in the range of 1kHz - 1MHz.

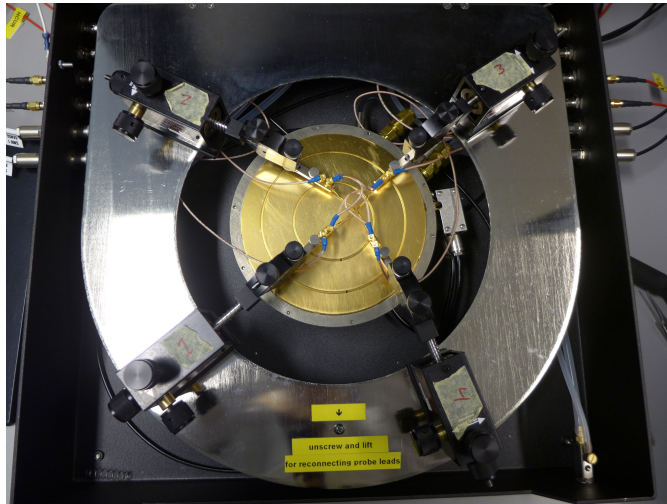


Figure 4.5: *The probe station used to perform CV measurements.*

Results and Discussion

The results of this work are divided into two parts. In section 5.1, the properties of the as-deposited sample set are examined. This includes optical characterization of the thickness and absorption in the SiN_x films (section 5.1.1), determination of Q_f (section 5.1.2), and the initial charge carrier lifetime in the silicon substrate (section 5.1.3).

Next, work was done to further increase Q_f in the SiN_x films by bias injection. Section 5.2 describes the results of the charge injection study, including an experimental investigation of the impact of Q_f on the SRV at the SiN_x-Si interface.

5.1 Initial Characterization

5.1.1 Optical Characterization

Thickness and Refractive Indices

The thicknesses and real refractive indices n of the SiN_x films determined using ellipsometry are summarized in Table 5.1 below:

Sample	Thickness [nm]	$n(\lambda = 600 \text{ nm})$
1	125	2.05
2	124	1.93
3	87	1.92

Table 5.1: Ellipsometrically measured thicknesses and refractive indices of the samples.

The values in Table 5.1 correspond well with the nominal values given in Table 4.3 based on previous knowledge of the reactor.

Absorption

In order for SiN_x to be applied in the PQED, the absorption in the film needed to be quantified. This is so that a correction factor to the non-ideal responsivity (as in equation 2.3) can be estimated for absorption in the film.

The complete complex refractive index as determined with ellipsometry in the range $\lambda = 300 - 1000\text{nm}$ can be found in the Appendix. As indicated in equation 2.6, the imaginary part of the refractive index k can be used to find the absorption coefficient α , and the attenuation of an incident beam can thus be calculated.

Figure 5.1 below shows the relative fraction of incident light absorbed in the films, calculated using equation 2.5. The figure only shows wavelengths up to 450 nm because beyond this point there was no measurable absorption in any of the films.

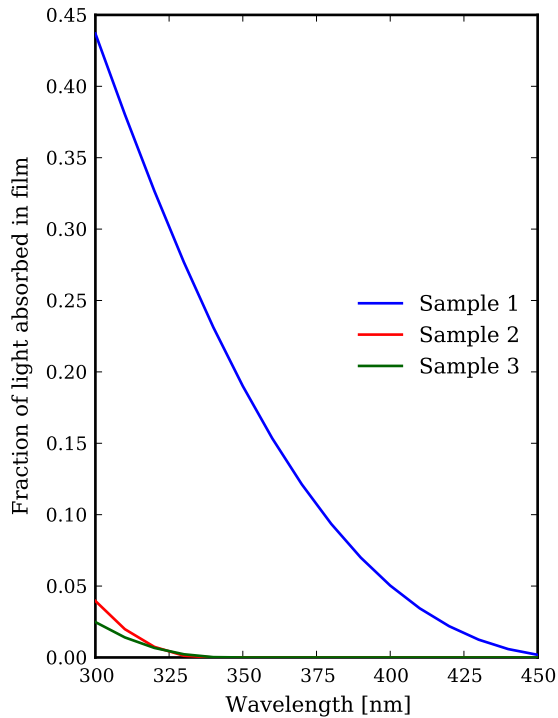


Figure 5.1: The fraction of incident light absorbed in the SiN_x films as a function of the wavelength λ .

As the applicable range is $\lambda = 400 - 800\text{ nm}$, samples 2 and 3 are well suited to the PQED in terms of absorption. The difference in relative absorption in samples 2 and 3 is simply due to the difference in thickness. The measurement uncertainty of the ellipsometric fit was not determined as a part of this work, but must be determined accurately for the PQED application.

5.1.2 CV characterization

A CV sweep of each of the electrodes on samples 1, 2 and 3 was performed. Many of the electrodes were defective, either due to pinholes or other defects in the nitride. Functioning electrodes were probed at 100kHz, 10kHz and 5kHz.

One common characteristic noted in all three samples was the dependency of the insulator capacitance C_i level on the frequency used to sweep the electrode. This indicates a high series resistance that retards the capacitance charging at high frequencies, effectively damping the measured capacitance by not allowing complete charging during each cycle at higher frequencies. In this respect, the lowest frequency measurements (5kHz) give the more accurate insulator capacitance. However, the sweeps at 10 kHz tended to be less noisy than those at 5kHz. The standard measurement frequency used on the CV wafers was thus chosen to be 10 kHz unless otherwise noted.

Due to issues of hysteresis in the SiN_x films, the most accurate picture possible of the films was given by not applying any positive bias. As K-centers can also be negatively charged, positive bias could have lead to negative charge retention. All of the CV sweeps were thus started at 0 V. The voltage was then taken down to -10 V in a number of steps (typically around -0.1 V per step), and then back up to 0 V in a reverse sweep.

Varying the AC voltage amplitude and sweep delay did not significantly alter the CV curves. Unless otherwise noted, an AC voltage amplitude of 30 mV and sweep delay of 0.1 s were used.

The following figures show a typical initial sweep for each of the samples.

Sample 1

Sample 1 (Fig.5.2) exhibited the largest amount of hysteresis of the three samples. The 10kHz sweep in Fig. 5.2 was the first sweep of that particular electrode, and we see a shift of around -2 V between the forward and reverse sweep. The hysteresis in the latter 5kHz and 100kHz sweeps is much less and leads to a much smaller shift in the flatband voltage than the initial sweep.

The elevated capacitance level compared to an ideal MIS capacitor in the 0 to -4 V region of the sweep is an artefact of series resistance due to the high resistivity of the wafers on which the films are deposited.

Sample 2

Sample 2 (Fig.5.3) exhibited the least amount of hysteresis of the three samples. The CV curves are not horizontally shifted relative to each other in any of the three subsequent sweeps shown in Fig. 5.3. This indicates that the fixed charge in this nitride is more stable.

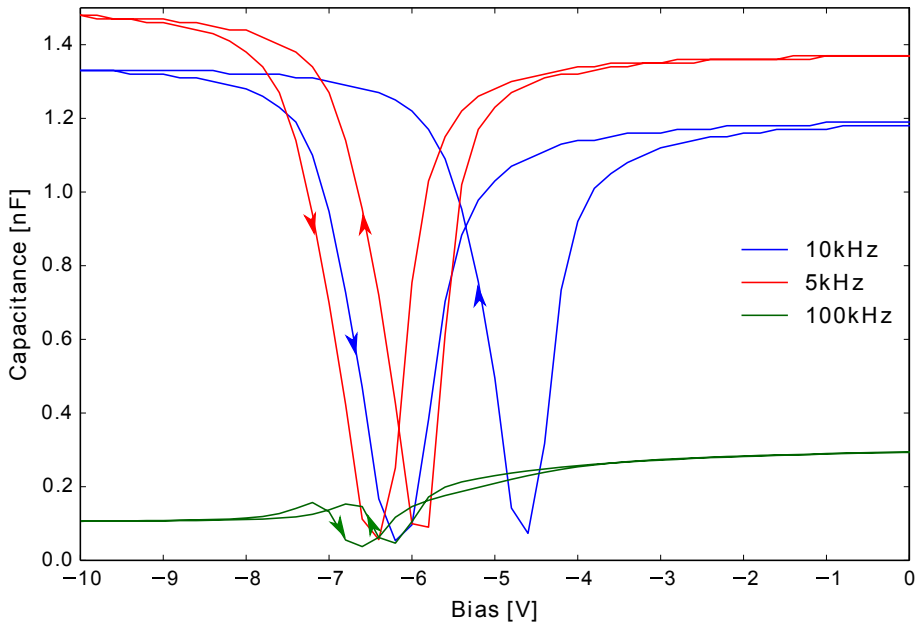


Figure 5.2: A typical initial CV sweep of sample 1.

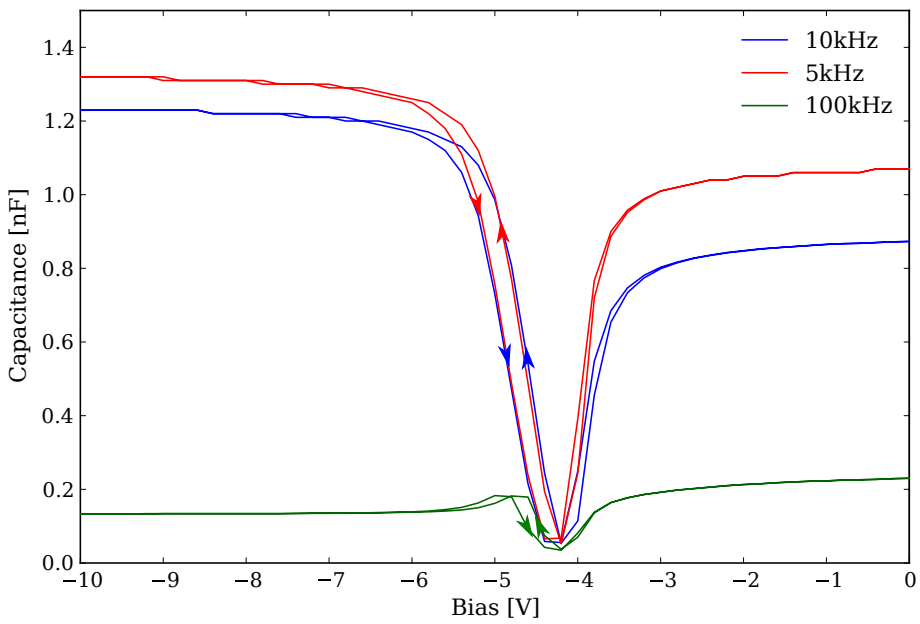


Figure 5.3: A typical initial CV sweep of sample 2.

The composition of sample 2 is more Si-rich than sample 1. The difference in hysteresis correlates well with the findings of Garcia et al., who showed that the hysteresis effect increases strongly with the nitrogen content in SiN_x [12].

Sample 3

Samples 2 and 3 were deposited using the same deposition parameters, and thus are chemically similar within variations in the deposition chamber. They differ, however, in their deposition time and thus thickness. The hysteresis loop in sample 3 was generally observed to be slightly larger than in sample 2, but as in sample 2, no significant flatband shift was found in sample 3 during initial characterization.

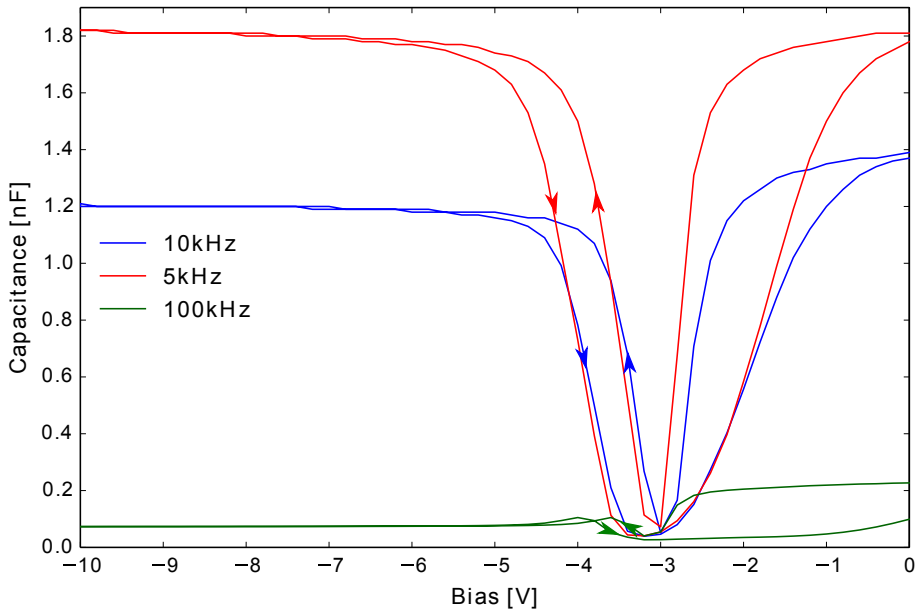


Figure 5.4: A typical initial CV sweep of sample 3.

Statistical analysis

Not all of the electrodes on each CV sample yielded good CV measurements. In fact, a majority of electrodes suffered from leakage and noise. There were two ways in which a CV sweep would show a malfunctioning electrode. In the case of fatal dielectric failure, the capacitance signal would typically become negative, which is unphysical, and sometimes oscillate between large negative and positive values.

The electrodes could also partially fail, in which case the C_1 level would typically slant downward. Figure 5.5 shows a typical CV sweep of an electrode in partial failure.

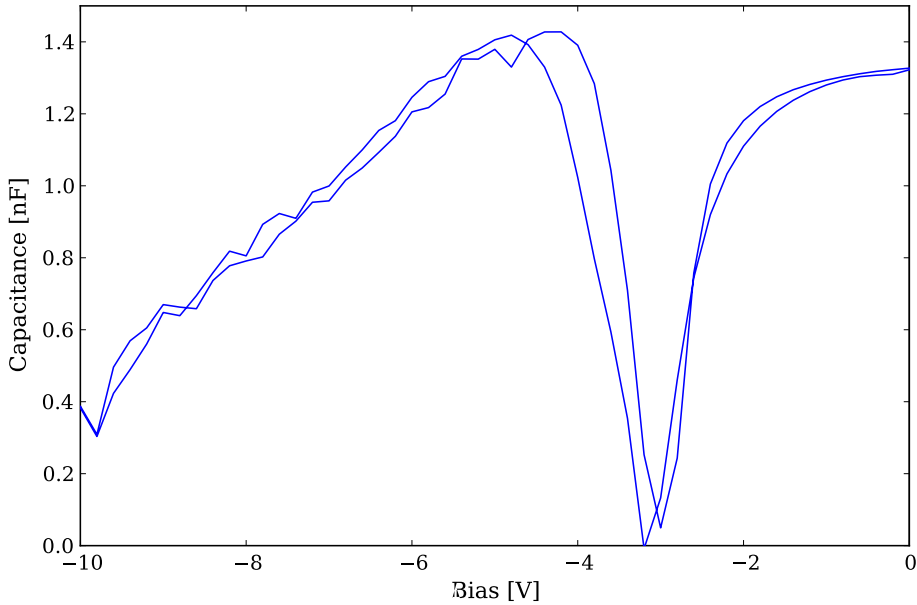


Figure 5.5: A typical CV sweep of a partially failed electrode.

Based on the data from the functioning electrodes at 10kHz, the average charge Q_f in each SiN_x film was determined. Table 5.2 below summarizes the findings of the investigation of all 56 of the electrodes of each sample.

	Sample 1	Sample 2	Sample 3
<i>Functioning electrodes</i>	34.5%	37 %	16 %
<i>Average Q_f [cm^{-2}]</i>	1.3×10^{12}	9.8×10^{11}	9.1×10^{11}
<i>Std dev of Q_f [cm^{-2}]</i>	7×10^{11}	4.8×10^{11}	4×10^{11}

Table 5.2: Percentage of electrodes without leakage, average Q_f and the standard deviation of Q_f statistically calculated over the 56 electrodes of each sample.

The percentage of functioning electrodes was significantly lower in sample 3, which was much thinner than samples 1 and 2. The large number of failed electrodes can likely be attributed the lower thickness of the film, which allows defects to lead to failure more easily.

5.1.3 Intial lifetime characterization

QSSPC

The charge-carrier lifetimes of the lifetime wafers of samples 1, 2, 3 and the lifetime reference sample were quantified using quasi-transient and quasi-steady state QSSPC measurements. Table 5.3 summarizes the results of the QSSPC measurements.

Both transient and steady-state measurements are performed on the basis of simplifications to the continuity equation, as described in section 3.2.1. The difference in the measured τ_{eff} values between the two types of QSSPC measurements show the fallacy in each of these simplifications, as well as random measurement error.

Sample	Steady-state QSSPC τ_{eff} [μs]	Transient QSSPC τ_{eff} [μs]	Average [μs]
1	546	579	562 ± 23
2	1040	1010	1025 ± 21
3	593	611	602 ± 12
Lifetime reference	3137	3170	3153 ± 23

Table 5.3: The effective carrier lifetimes at $\Delta n = 10^{15}$ as measured using QSSPC.

The lifetime wafer of sample 2 was observed to have an unusually high lifetime. Repeated measurements at different areas of the wafer confirmed that this was the case. This shows a certain variability in the PECVD process.

The passivation of all of the samples is quite good. τ_{eff} in all of the samples exceeds τ_{eff} measured in the previous PQED [18].

The effective lifetime τ_{eff} of a sample is a function of the bulk and surface lifetimes. As the influence of the fixed charge Q_f is solely on the surface recombination properties, we would like to separate out the contribution of the bulk lifetime. The lifetime reference sample was passivated with a-Si, a good passivator with no fixed charges. We then assume that the passivation is so good that τ_{eff} is bulk recombination limited. Due to the fact that the SRV likely does contribute to τ_{eff} , equation 3.7 shows that the measured τ_{eff} represents the lower limit of the actual bulk lifetime τ_{bulk} . We can thus conclude that τ_{bulk} in this wafer set is at least 3.1 ms.

Using the estimated τ_{bulk} and equation 3.9, the SRV of each sample may be estimated. Table 5.4 below summarizes the average SRV calculated from the quasi-transient and steady-state QSSPC measurements, based on the previously described assumptions.

Sample	SRV [cm s^{-1}]
1	37
2	17
3	34

Table 5.4: The average SRV based on QSSPC measurements.

These SRV values are low but not extraordinarily so. For reference, some of the lowest SRVs reported are in the order of 2 cm/s [9]. The estimated SRVs in Table 5.4 are already at the lower end of the simulation plotted in Fig.2.11 and thus are low enough to facilitate a high QE.

PL

Figure 5.6 shows the calibrated PL images of the lifetime wafers of sample 1, 2 and 3 as well as the lifetime reference. Note the difference in scale bars in each of the figures.

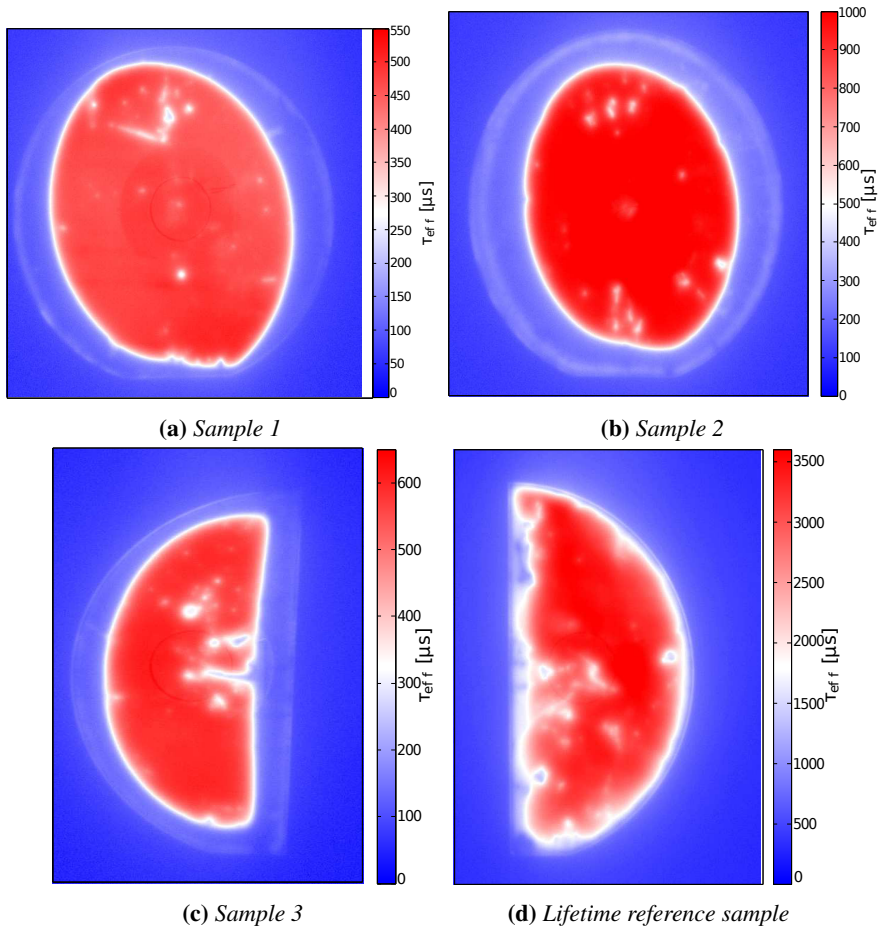


Figure 5.6: Calibrated PL images of the lifetime samples.

PL imaging confirms that the visible defects in the a-Si as seen in Fig. 4.1 affect the effective lifetime. The actual wafer edge in Figs. 5.6a - 5.6c are the blue borders that can be seen approximately 1 cm from where the red area ends. The area of degraded lifetime around the wafer edge corresponds in size with the impurities seen on the backside of the wafers.

Outside of the area of degraded a-Si, the wafers can be seen to have homogeneous lifetime. The white marks visible on the images are due to scratches acquired during handling.

5.2 Charge Injection Analysis

The initial characterization of the nitrides showed a fixed charge Q_f in the range of $0.9 - 1.3 \times 10^{12} \text{cm}^{-2}$. We will now explore the possibility of further increasing Q_f by means of applying a large negative bias.

5.2.1 Charging Injection Study

Charge was injected into the SiN_x films using the CV set-up. A presoak voltage up to $\pm 30\text{V}$ may be applied, as well as a hold time at a designated presoak voltage. Immediately after the bias soak, a CV sweep would be performed to determine the change in Q_f .

Charging Time

Figure 5.7 below shows the dependence of the measured Q_f on the hold time at the soaking bias. A presoak voltage of -30V was used as this is the highest available internally on the Keithley CV setup.

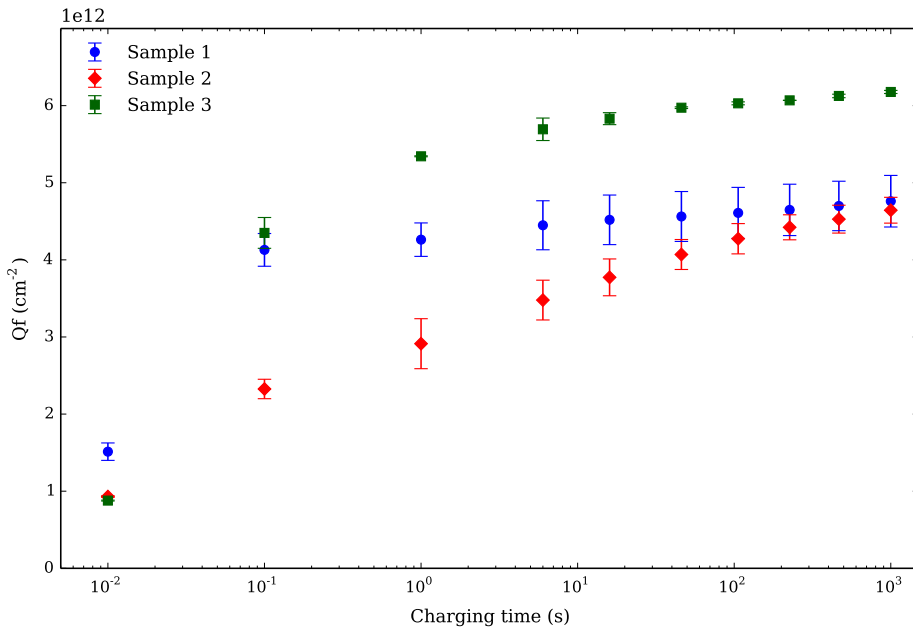


Figure 5.7: The charge Q_f measured as a function of the biasing time at -30V .

The points of samples 1 and 2 represent the average and standard deviations of measurements performed on three electrodes. Sample 3 only represents two electrodes, as a fewer number of electrodes were available for measurement.

Figure 5.7 shows that Q_f increases rapidly as a function of bias soaking time before it saturates after approximately 100 seconds. Q_f continues to increase slightly after this

point. However, for practical applications we assume that Q_f does not increase significantly beyond 100s at -30V.

Furthermore, sample 3 was observed to converge to a higher Q_f value than samples 2 and 1. A study of a greater number of electrodes would be required to confirm whether this is a property of sample 3 or simply due to local variations.

Charging Bias

Figure 5.8 shows the dependence of Q_f on the soaking bias. Soaking started at -5 V and was incrementally negatively increased, so that the graph should be interpreted from right to left. The hold time was 70 seconds at each soaking bias. As seen in Fig. 5.7, the films can be assumed to be saturated at this point.

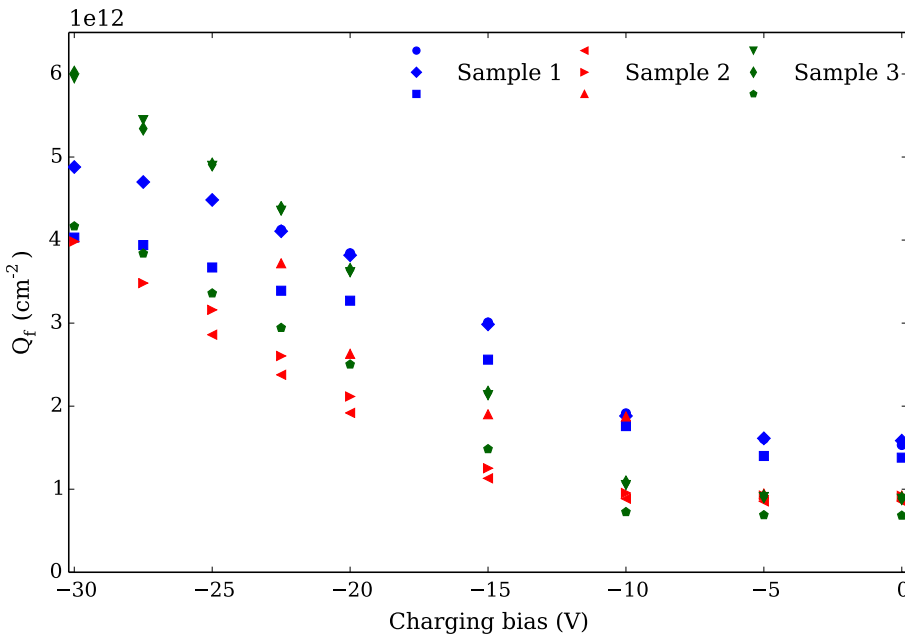


Figure 5.8: The charge Q_f measured on the samples after biasing for 70 s at a soaking bias.

Q_f is constant until the soaking bias reaches -10 V. This is at least partially an artifact of CV characterization. The initial sweeps performed on the samples, as discussed in section 5.1.2, involve biasing the sample down to -10 V. A full CV sweep takes less than a minute, and so the time spent at each bias point is minimal. Even so, the samples have been partially saturated at -10 V when the experiment shown in Fig.5.8 began.

At soaking biases exceeding -10 V, Q_f increases linearly. Several of the electrodes experienced dielectric breakdown as the voltage was increased, which is why the data abruptly stop for several of the series. Increasing the electric field across the dielectric increases the probability of charges tunneling across the energetic barrier at the SiN_x -Si interface and hence conducting current.

In Fig.5.8, we see clearly that Q_f is still increasing at -30 V. Elmiger et al. [10] demonstrated that the density of K-center defects extends up to 20 nm into SiN_x films. This means that there are a limited number of defects, so in theory all of the defects could be filled and absolute saturation achieved. Further experimentation is necessary to determine the magnitude of Q_f at absolute K-center saturation. This may also be difficult to find, as the number of electrodes that undergo dielectric breakdown is expected to increase as the absolute value of the soaking bias increases.

Stability Over time

In order for a PQED structure based on SiN_x films to remain predictable over time, Q_f must be stable. A set of CV electrodes were charged to saturation at -30V and measured at random intervals ranging from 1 to 12 days for up to 50 days. Between measurements, the samples were stored in the dark.

The insulator capacitance C_i would occasionally be vertically shifted in between measurements, which can be attributed to instabilities in the CV set-up. C_i was kept constant in the Q_f calculation over the course of these measurements to avoid problems due to this artifact.

Figure 5.9 below shows the evolution of the injected charge Q_f over the measurement period.

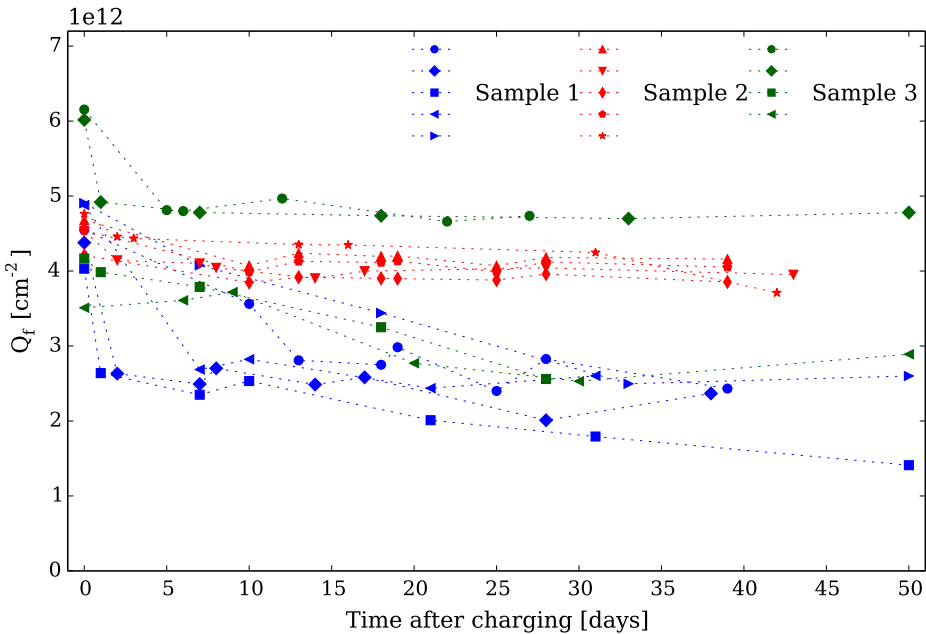


Figure 5.9: Stability of the induced charge Q_f measured on the samples that had been charged to saturation at -30 V and then measured successively for up to 50 days.

Several key features of Fig. 5.9 should be noted. First of all, all of the electrodes

on sample 1 initially decay quickly, but the charge consistently increases on every other measurement. At this point it is useful to remember that the SiN_x film on sample 1 is prone to hysteresis (see Fig.5.6a). Each point in Fig. 5.9 was calculated based on a CV sweep down to -25 V, as the flatband voltage was typically close to -19 V at saturation. In sample 1, however the flatband voltage had typically become less negative during the rest period and was shifted significantly. Thus a sweep down to -25 V was enough to recharge the film again, thereby increasing the value of Q_f in the subsequent measurement.

Figure 5.10 shows a typical hysteresis loop seen in sample 1 during stability measurements. The flatband voltage is shifted by approximately -4 V between the forward and reverse sweeps.

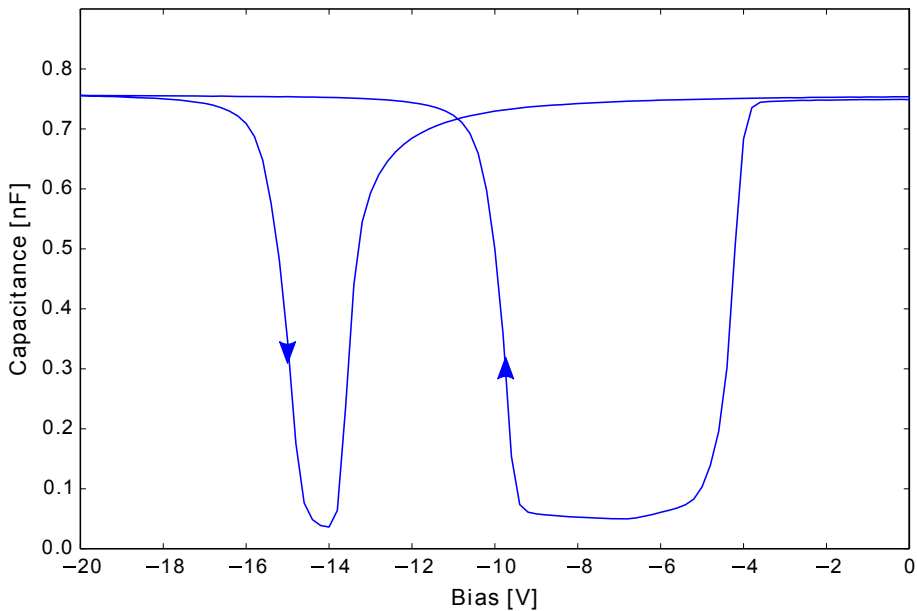


Figure 5.10: A typical CV sweep of sample 1 during the charge stability study.

Based on the general downward trend of Q_f measured in the CV wafer of sample 1, it is postulated that Q_f is leaking out of the film and decaying towards the original value of $Q_f = 1 \times 10^{12} \text{cm}^{-2}$. Leaving an electrode alone for an extended period of time without remeasurement, perhaps 20 - 30 days, would be necessary to confirm this theory. The electrode denoted with square, blue points was left for almost 20 days before the final measurement, and Q_f is nearly $1 \times 10^{12} \text{cm}^{-2}$ in this case.

Q_f in samples 2 and 3 is far more stable. In sample 2, Q_f is constant within measurement uncertainty for the entire period. In sample 3, Q_f decreases quickly during the first few days before all of the electrodes stabilizing. There is a larger variation in the Q_f value at which the electrodes in sample 3 settle.

Summary

The fixed charge Q_f has been increased to up to $6 \times 10^{12} \text{cm}^{-2}$ by charge injection via bias soaking. The films are saturated after approximately 100 s at a soaking bias of -30 V. The fixed charge Q_f has been shown to increase linearly with soaking bias, and is not saturated at -30 V. Charge retention has been demonstrated over a period of up to 50 days, and the stability is particularly good in sample 2. As sample 2 seems to have the most promising properties, this sample was used in the subsequent investigation of the SRV - Q_f relation.

5.2.2 SRV-Fixed Charge Analysis

Q_f is a source of field-effect passivation, and thus affects the SRV at the SiN_x -Si interface. As discussed in section 2.3.4, the SRV contributes to the quantum deficiency of the PQED. It is therefore of interest to investigate the relationship between Q_f in the SiN_x and the SRV at the SiN_x -Si interface.

Three electrodes on the PL/CV wafer of sample 2 were injected with charge using the CV set-up. They were soaked for 100 s in steps of -1V from -10V to -30V. Between each bias point, the PL/CV wafer was imaged in the PL set-up.

The large, 8mm electrodes on the PL/CV wafer (as shown in Fig.4.2b) had larger substrate series resistance than the CV wafers. The C_i dependence on the AC probe voltage was even more apparent, so the best CV signal was at the lowest possible AC frequency, 1kHz, with an AC probe amplitude of 100mV.

Figure 5.11 shows how the flatband voltage in the CV sweeps shifted as a result of soaking, with corresponding PL images. It should be interpreted from right to left. The PL images are calibrated and all have the same color bar scale, so that darker red indicates a longer τ_{eff} . The circles in the upper left corner of each image are the electrodes being charged, whereas the other three visible circles are untouched electrodes.

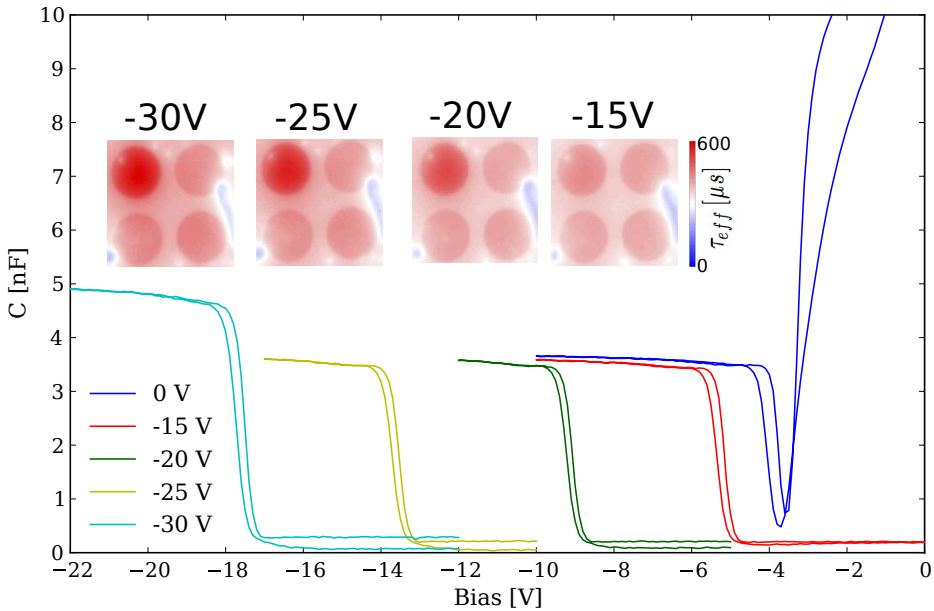


Figure 5.11: Post-bias CV sweeps with corresponding PL images showing the increase in Q_f .

Bias soaking combined with CV sweeps and PL imaging gave qualitative data on the relationship between Q_f and τ_{eff} .

Effective lifetime

The PL images were subsequently calibrated and Q_f extracted from the corresponding CV curves. Figure 5.12 shows the experimentally measured relationship between τ_{eff} and Q_f .

As expected, τ_{eff} increases as a function of Q_f . This indicates an increased field-effect passivation which decreases the SRV at the SiN_x -Si interface.

The difference in τ_{eff} between the three electrodes may be attributed to inhomogeneities in the film as well as small fluctuations in the placement of the wafer in the PL set-up.

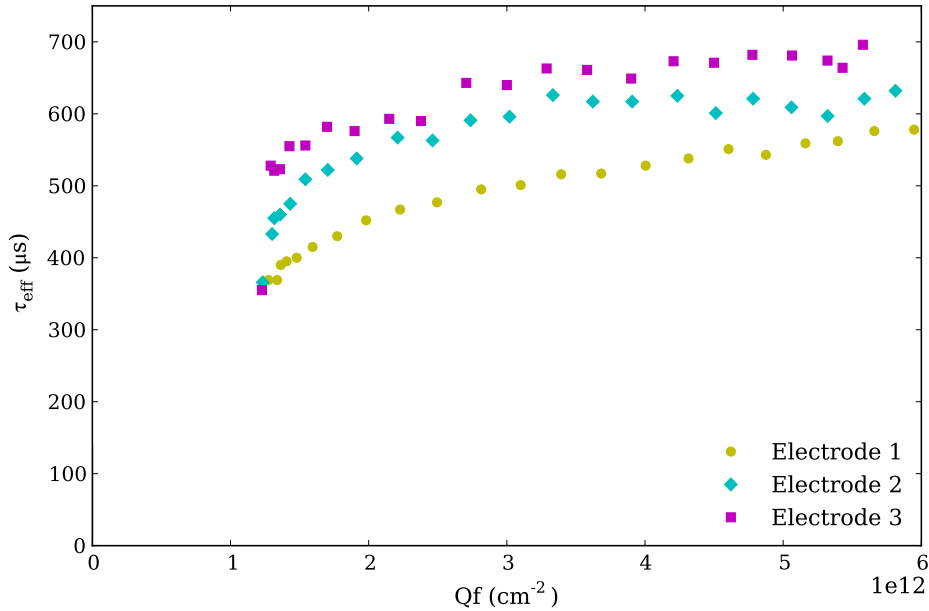


Figure 5.12: τ_{eff} as a function of Q_f as measured by dual the CV/PL characterization for three electrodes of the CV/PL wafer of sample 2.

Surface recombination

Extracting the SRV based on the τ_{eff} data was less straightforward. The anneal required to contact the backside of the wafer with circular aluminum electrode degraded the a-Si passivation. τ_{eff} measured by QSSPC decreased from 1187 μm to 415 μm post-anneal. It is no longer safe to assume that the SRV of the a-Si backside is negligible.

To give a picture of the range of the front SRV, best and worst case estimates for the a-Si-Si interface SRV were used. The worst case is that the a-Si passivation has barely been degraded, so that almost all of the recombination is due to the SiN_x -Si interface. In this case we assume $\text{SRV}_{\text{back}} = 10\text{cm s}^{-1}$. In the best case for the SiN_x , we assume that the a-Si has been degraded to a large degree so that $\text{SRV}_{\text{back}} = 50\text{cm s}^{-1}$. The SRV at the SiN_x -Si interface, $\text{SRV}_{\text{front}}$, was then calculated assuming asymmetric surface recombination [21].

Figure 5.13 shows the best- and worst-case $\text{SRV}_{\text{front}}$ for each of the three electrodes measured. The points are the experimental data while the dashed lines are theoretical fit.

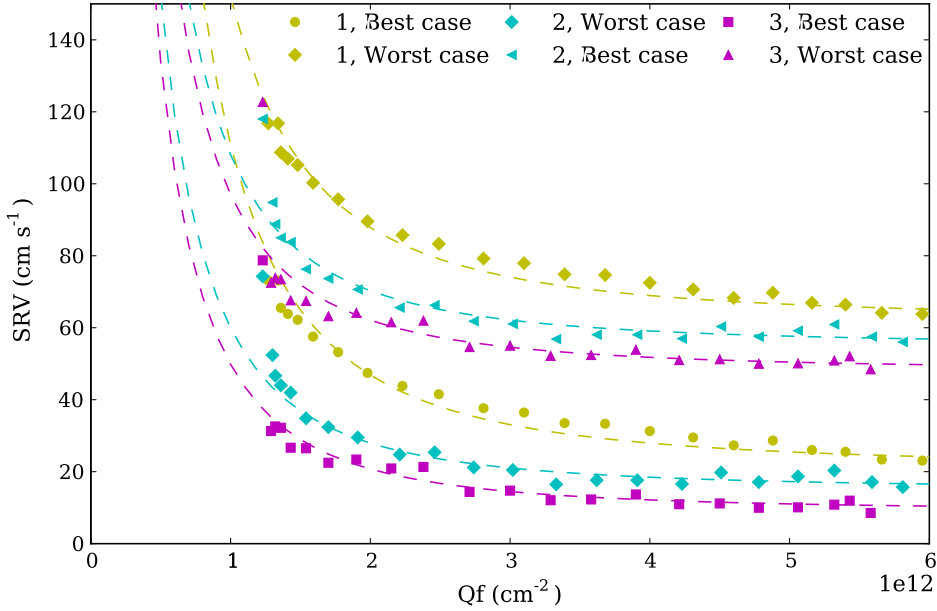


Figure 5.13: The best and worst case SRVs of each of the three electrodes measured, fitted using extended SRH formalism and the sub-surface damage theory.

The SRV data was fitted using the extended SRH formalism by varying S_{p0} as discussed in section 2.3.4. An injection level of $\Delta n = 3.1 \times 10^{14} \text{cm}^{-3}$ was found when calibrating the PL data and subsequently used in this model.

It was found that the data could not be fitted using extended SRH formalism alone. The Girisch model predicted that the SRV should drop even more for high values of Q_f . The discrepancies of SRV values with SRH formalism, especially at lower injection levels ($\Delta n < 10^{15} \text{cm}^{-3}$), have previously been reported [41, 17].

Steingrube et al.[41] postulate that hydrogen is released into the Si wafer during SiN_x deposition. The density of this hydrogen is such that the covalent bonds of Si are weakened, causing lattice defects. This in turn degrades the bulk lifetime near the SiN_x -Si interface, in a region called the *sub-surface damage region*.

The elevated SRV relative to the theoretically predicted SRV may thus be attributed to sub-surface damage which occurs in the PECVD deposition. This damage may be modelled by adding an extra, constant SRV term which is uninfluenced by Q_f . The modelled SRV is then given by the equation:

$$\text{SRV}_{\text{front}} = S_{\text{SRH}}(Q_f, S_{p0}) + S_{\text{damage}} \quad (5.1)$$

Table 5.5 summarizes the fit parameters specified in equation 5.1 used to calculate the dashed theoretical fit curves in Fig.5.13. The fit was performed using trial-and-error with the two parameters.

Electrode	Condition	S_{p0} [cms^{-1}]	S_{damage} [cms^{-1}]
1	Best case	1.1×10^6	21
	Worst case	1.1×10^6	62
2	Best case	5.5×10^5	15
	Worst case	6×10^5	55
3	Best case	5×10^5	9
	Worst case	6×10^5	48

Table 5.5: *The fit parameters for the theoretical model of $SRV(Q_f)$ given in equation 5.1.*

The difference between the fit of the best- and worst-case estimates of SRV_{back} in each case is the S_{damage} term. Since the S_{p0} term is nearly constant in the two estimations, we reason that the values obtained are close to the actual S_{p0} values in the SiN_x film. The average value was found to be $S_{p0} = 7.4 \times 10^5 \text{cms}^{-1}$, with a standard deviation of $\sigma = 2.8 \times 10^5$. This is in the mid range of feasible S_{p0} values, as plotted in Fig.2.10.

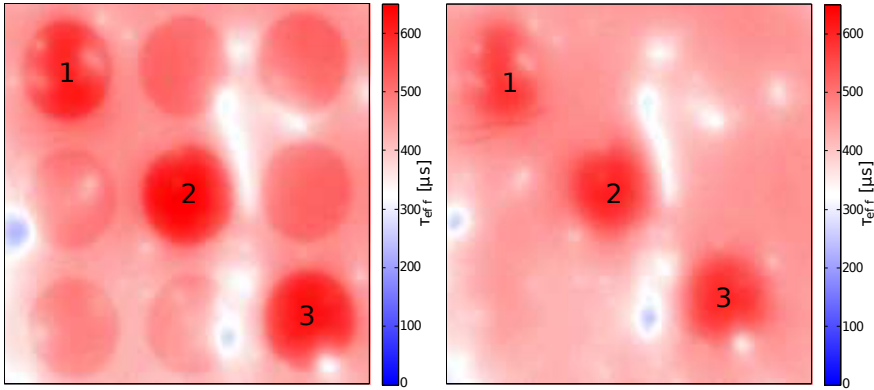
Despite of the sub-surface damage, the SRVs achieved can be said to be low enough for the application. However, the sub-surface damage likely degrades the predictability of the system and should thus be addressed. Additionally, achieving the lowest SRV possible will further improve the QE. The sub-surface damage term could be reduced by using a remote plasma PECVD reactor rather than the direct plasma reactor used to deposit the SiN_x films in this work [6].

5.2.3 Electrode removal

The surface of a photodetector must be transparent to photons in the applicable wavelength range. Thus far we have shown that a high Q_f can be achieved by the means of applying large negative soaking biases across the film using metal electrodes. We have also demonstrated that Q_f is stable over time. In order for this SiN_x charging technique to be used for fabricating induced diode PQEDs, we would like to show that the charges are still present once the metal electrodes are removed.

After the three electrodes on the PL/CV wafer of sample 2 were charged to -30 V, a final PL image was taken of the sample. The image was later corrected for reflection in the aluminum electrodes. The aluminum was then stripped in a bath of 85% concentrated phosphoric acid. The sample was kept in the bath until the electrodes were visibly removed, which took about 40 minutes. The wafer was then imaged again in order to verify the continued presence of Q_f .

Figure 5.14 shows the PL image before and after the electrodes were strip. The charged electrodes have been labeled 1 - 3 for convenience.



(a) Calibrated PL image of the sample before the electrode removal. (b) Calibrated PL image of the sample after electrode removal.

Figure 5.14: Calibrated PL images before and after electrode removal.

Figure 5.14 clearly shows the continued presence of Q_f after the removal of the electrodes. Table 5.6 shows PL measured τ_{eff} at each of the electrodes before and after the electrodes were stripped.

Electrode nr	τ_{eff} , before strip [μs]	τ_{eff} , after strip [μs]
1	588	552
2	632	591
3	613	580

Table 5.6: The effective lifetimes before and after electrode removal.

τ_{eff} decreases slightly in all three areas after electrode removal. As previously mentioned, reflection in the electrodes is compensated for by introducing a calibration factor based on the difference in counts between a PL image with and without aluminum foil in the back. This calibration factor likely undercompensates for the increased apparent lifetime due to the electrodes. We will therefore infer that the decrease in lifetime is a PL imaging artifact rather than charge degradation.

It is feasible that a layer of aluminum could be applied during detector processing, used to charge the SiN_x film, and then removed. According to Williams et al.[48], the ratio of etch rates of SiN_x to Al in concentrated phosphoric acid is approximately 1:490. As charge injection in the SiN_x occurs within the first 20 nm of the SiN_x -Si interface, the phosphoric acid strip should not affect these charges, and does not appear to in this initial experiment.

Conclusion

This work has examined amorphous PECVD silicon nitride as a replacement for thermal silicon oxide in the predictable quantum efficient detector (PQED) application. The fixed charge Q_f in the dielectric top coat of the PQED induces inversion and hence a rectifying junction in the silicon substrate. The magnitude of Q_f thus determines the magnitude of band-bending in the substrate and is of the utmost importance to the induced diode. Simulations have shown that increasing Q_f will increase the surface recombination velocity at the SiN_x -Si interface via field-effect passivation. Furthermore, an increased Q_f will increase the quantum efficiency of the detector at higher optical power.

A sample set consisting of 120 nm of one Si-rich ('sample 1') and one N-rich ('sample 2') SiN_x were deposited on high resistivity, p-type Cz wafers. The N-rich nitride was additionally deposited in an 80 nm thickness ('sample 3'). As expected, the N-rich SiN_x behaved as a more ideal dielectric both optically and electrically. All films demonstrated high lifetimes as-deposited. MIS capacitors were created from each of the samples for CV characterization.

The intrinsic fixed charge in the as-deposited SiN_x was found to be around $Q_f = 1 \times 10^{12} \text{cm}^{-2}$, which in itself represents an order of magnitude increase from as-deposited SiO_x . The intrinsic fixed charge was largest in sample 2. The optical absorption in samples 2 and 3 in the $\lambda = 400 - 800 \text{nm}$ range was shown to be $\ll 1\%$ while it was significantly larger in sample 1.

The samples were further charged by applying a soaking bias of up -30 V across the MIS capacitors. Q_f was shown to increase to saturation in approximately 100 s at -30 V. Q_f increased linearly as a function of soaking bias to $Q_f = 4 - 6 \times 10^{12} \text{cm}^{-2}$ depending upon the electrode and was not saturated at -30 V, so that Q_f could likely be further increased by applying larger soaking biases. Q_f was shown to be stable in samples 2 and 3 within measurement uncertainty for a period of up 50 days, whereas Q_f in sample 1 decreased significantly over time. Their stability under illumination and temperature fluctuations has yet to be characterized.

Next, the relation between the SRV and Q_f has been investigated experimentally by means of dual CV/PL characterization. As theoretically predicted, the SRV has been shown

to decrease significantly with increased Q_f . However, the curves could not simply be fit to the extended SRH model, as the terminal values of the SRV at high Q_f were significantly larger than predicted by this model. An extra term, denoted S_{damage} , has been added in order to fit the measurement. It has been inferred that sub-surface damage caused by PECVD processing creates a density of impurity states in the band gap near the SiN_x -Si interface which causes increased SRH recombination in this area of the wafer.

Finally, the continued presence of Q_f after the removal of the Al electrodes was demonstrated. This leads us to suggest SiN_x films could be biased to high Q_f , after which the electrodes could be removed to allow the film to be used in the front surface of the PQED. An increase from $Q_f = 4 \times 10^{11} \text{cm}^{-2}$ in SiO_x of the original PQED [39] to $Q_f \geq 6 \times 10^{12} \text{cm}^{-2}$ may thus be achieved. Q_f can also potentially be varied using applied bias to suit the needs of the PQED.

We thus conclude that SiN_x is a strong candidate for application in the PQED. However, uncertainty issues in the film absorption and the overall charge stability need to be examined before SiN_x is used.

Suggestions for further work

A number of loose ends need to be tied up to further determine the usefulness of SiN_x in the PQED application. The following non-exhaustive list suggests topics of research to further explore the application of SiN_x in induced diode photodetectors.

Charge stability: The fixed charge Q_f in the nitride has been shown to be stable over time. Application in a photodetector, however, also requires it to be stable under both varying temperatures and illumination. There is reason to believe that UV light could upset the charge in the film [25]; however, to the knowledge of the author there is no information about the long term effects of illumination at $\lambda = 400 - 800\text{nm}$. Furthermore, Q_f should be measured at 77K, as this is the purposed operating temperature for high accuracy measurements with the PQED [18].

Optical properties: A more accurate characterization of the absorption in the SiN_x film would be necessary before SiN_x could replace SiO_x in the PQED. Although we have shown that there is far less than 1% absorption on the applicable range for the best film, the absorption needs to be known in ppm and the uncertainty quantified to give a correct estimate of the responsivity.

Optimization of chemical composition: Only two chemically different nitrides have been investigated in this work. Of the two, the N-rich film was shown to have superior properties in terms of charge retention and optical absorption. The optical and electrical characteristics of PECVD SiN_x films are known to vary greatly with deposition parameters [32, 28, 27, 12]. A variety of SiN_x films should be fabricated with the goal of optimization both in terms of charge retention and optical absorption.

Charging saturation: Q_f was increased to $6 \times 10^{12}\text{cm}^{-2}$, but as shown in Fig.5.8 had not been saturated at a soaking bias of -30V. Although an increased soaking bias also increases the likelihood of dielectric failure, it may also allow the further increase of Q_f . Work should be done to find the absolute saturation charge of SiN_x.

Homogeneity of bias charging for large areas: If the method purposed is to be used in the PQED, an area of $1 \times 2\text{cm}^2$ would need to be injected with charge. An investigation

should be made as to whether soaking such a large area will cause the film to be charged homogeneously. The sequential CV soaking and PL imaging technique demonstrated in section 5.2.2 might be used to this end.

Decreasing the SRV by avoiding sub-surface damage: It was concluded that the sub-surface damage issues encountered in the Q_f -SRV analysis could be remedied by depositing the SiN_x films in a remote plasma reactor [6]. This should be tested experimentally.

Bibliography

- [1] Atlas website. http://www.silvaco.com/products/tcad/device_simulation/atlas/atlas.html. Accessed: 06.04.14.
- [2] Cogenda website. <http://www.cogenda.com/article/Genius>. Accessed: 08.06.14.
- [3] Quantum Candela - Project Outline. <http://www.quantumcandela.net/project.html>. Accessed: 25.04.14.
- [4] Armin G. Aberle. *Crystalline Silicon Solar Cells: Advanced Surface Passivation and Analysis*. 2004.
- [5] Armin G. Aberle, Stefan Glunz, and Wilhelm Warta. Impact of illumination level and oxide parameters on ShockleyReadHall recombination at the Si-SiO₂ interface. *Journal of Applied Physics*, 71(9):4422, 1992.
- [6] Armin G. Aberle and R Hezel. Progress in Low-temperature Surface Passivation of Silicon Solar Cells using Remote-plasma Silicon Nitride. *Progress in Photovoltaics*, 5:29–50, 1997.
- [7] Qijin Cheng, Shuyan Xu, and Kostya (Ken) Ostrikov. Controlled-bandgap silicon nitride nanomaterials: deterministic nitrogenation in high-density plasmas. *Journal of Materials Chemistry*, 20(28):5853, 2010.
- [8] B. E. Deal, M. Sklar, a. S. Grove, and E. H. Snow. Characteristics of the Surface-State Charge (Q_{ss}) of Thermally Oxidized Silicon. *Journal of The Electrochemical Society*, 114(3):266, 1967.
- [9] G Dingemans and W M M Kessels. Status and prospects of Al₂O₃-based surface passivation schemes for silicon solar cells. 30(4):1–27, 2012.
- [10] J. R. Elmiger and M. Kunst. Investigation of charge carrier injection in silicon nitride/silicon junctions. *Applied Physics Letters*, 69(4):517, 1996.
- [11] Shizuo Fujita and Akio Sasaki. Dangling Bonds in Memory-Quality Silicon Nitride Films. *Solid-State Science and Technology*, pages 398–402, 1985.

-
- [12] S. Garcia, I. Martil, G. Gonzalez Diaz, E. Castan, S. Duenas, and M. Fernandez. Deposition of SiN_x:H thin films by the electron cyclotron resonance and its application to Al/SiN_x:H/Si structures. *Journal of Applied Physics*, 83(1):332, 1998.
- [13] Jon Geist. Complete collection of minority carriers from the inversion layer in induced junction diodes. *Journal of Applied Physics*, 52(7):4879–4881, 1981.
- [14] Jon Geist, Giorgio Brida, and Maria Luisa Rastello. Prospects for improving the accuracy of silicon photodiode self-calibration with custom cryogenic photodiodes. *Metrologia*, 40(1):S132–S135, February 2003.
- [15] T R Gentile, J M Houston, J E Hardis, C L Cromer, and a C Parr. National Institute of Standards and Technology high-accuracy cryogenic radiometer. *Applied optics*, 35(7):1056–68, March 1996.
- [16] Reinhard B M Girisch, Robert P Mertens, and Roger F D E Keersmaecker. Determination of Si-SiO₂ Interface Recombination Parameters Using a Gate-Controlled Point-Junction Diode Under Illumination. *IEEE Transactions on Electron Devices*, 35(2):203 – 222, 1988.
- [17] S W Glunz, D Biro, S Rein, and W Warta. Field-effect passivation of the SiO₂/Si interface. *Journal of Applied Physics*, 86(1):683 – 691, 1999.
- [18] Jarle Gran, Toomas Kübarsepp, Meelis Sildoja, Farshid Manoocheri, Erkki Ikonen, and Ingmar Müller. Simulations of a predictable quantum efficient detector with PC1D. *Metrologia*, 49(2):S130–S134, April 2012.
- [19] Martin A Green and Mark J Keevers. Optical Properties of Intrinsic Silicon at 300. 3(November 1994):189–192, 1995.
- [20] T.E. Hansen. Silicon UV-Photodiodes Using Natural Inversion Layers. *Physica Scripta*, 18:471–475, 1978.
- [21] Halvard Haug. *New Methods for Investigation of Surface Passivation Layers for Crystalline Silicon Solar Cells*. PhD thesis, 2014.
- [22] Halvard Haug, Ørnulf Nordseth, Edouard V. Monakhov, and Erik Stensrud Marstein. Photoluminescence imaging under applied bias for characterization of Si surface passivation layers. *Solar Energy Materials and Solar Cells*, 106:60–65, November 2012.
- [23] Sandra Herlufsen, Jan Schmidt, David Hinken, Karsten Bothe, and Rolf Brendel. Photoconductance-calibrated photoluminescence lifetime imaging of crystalline silicon. *physica status solidi (RRL) - Rapid Research Letters*, 2(6):245–247, December 2008.
- [24] Stian Samset Hoem, Jarle Gran, Meelis Sildoja, Farshid Manoocheri, Erkki Ikonen, and Ingmar Müller. Physics of self-induced photodiodes. (1):3–4.
- [25] Erwin P Jacobs and G Dorda. Charge storage by irradiation with UV light in non-biased MNOS structures. 20, 1977.

-
- [26] F. R. Libsch and J. Kanicki. Bias-stress-induced stretched-exponential time dependence of charge injection and trapping in amorphous thin-film transistors. *Applied Physics Letters*, 62(11):1286, 1993.
- [27] A. J. Lowe, M. J. Powell, and S. R. Elliott. The electronic properties of plasma-deposited films of hydrogenated amorphous SiN_x (0<x<1.2). *Journal of Applied Physics*, 59(4):1251, 1986.
- [28] Masahiko Maeda. Electrical properties and their thermal stability for silicon nitride films prepared by plasma-enhanced deposition. *Journal of Applied Physics*, 53(10):6852, 1982.
- [29] J E Martin, N P Fox, and PJ Key. A Cryogenic Radiometer for Absolute Radiometric Measurements. *Metrologia*, 21:147–155, 1985.
- [30] Ingmar Müller, Uwe Johannsen, Ulrike Linke, Liana Socaciu-Siebert, Marek Smíd, Geiland Porrovecchio, Meelis Sildoja, Farshid Manoocheri, Erkki Ikonen, Jarle Gran, Toomas Kübarsepp, Giorgio Brida, and Lutz Werner. Predictable quantum efficient detector: II. Characterization and confirmed responsivity. *Metrologia*, 50(4):395–401, August 2013.
- [31] Henning Nagel, Christopher Berge, and Armin G Aberle. Generalized analysis of quasi-steady-state and quasi-transient measurements of carrier lifetimes in semiconductors. *Journal of Applied Physics*, 86(11):6218–6221, 1999.
- [32] Haruo Nakayama and Tatsuya Enomoto. Effects of Nitride Deposition Conditions on Characteristics of an MNOS Nonvolatile Memory Transistor. *Japanese Journal of Applied Physics*, 18:1773–1779, 1979.
- [33] Jenny Nelson. *The Physics of Solar Cells*. 2003.
- [34] M. J. Powell. Charge trapping instabilities in amorphous silicon-silicon nitride thin-film transistors. *Applied Physics Letters*, 43(6):597, 1983.
- [35] Dieter K. Schroder. *Semiconductor Material and Device Characterization*. John Wiley & Sons, Inc., Hoboken, NJ, USA, October 2005.
- [36] D.K. Schroder. Carrier lifetimes in silicon. *IEEE Transactions on Electron Devices*, 44(1):160–170, 1997.
- [37] Meelis Sildoja, Timo Dönsberg, Henrik Mäntynen, Mikko Merimaa, Farshid Manoocheri, and Erkki Ikonen. Use of the Predictable Quantum Efficient Detector with Light Sources of Uncontrolled State of Polarization. *Meas. Sci. Technol.*, 25, 2013.
- [38] Meelis Sildoja, Farshid Manoocheri, and Erkki Ikonen. Reflectance calculations for a predictable quantum efficient detector. *Metrologia*, 46(4):S151–S154, August 2009.
-

-
- [39] Meelis Sildoja, Farshid Manoocheri, Mikko Merimaa, Erkki Ikonen, Ingmar Müller, Lutz Werner, Jarle Gran, Toomas Kübarsepp, Marek Smíd, and Maria Luisa Rastello. Predictable quantum efficient detector: I. Photodiodes and predicted responsivity. *Metrologia*, 50(4):385–394, August 2013.
- [40] R A Sinton, A Cuevas, and M Stuckings. Quasi-Steady-State PhotoConductance, A new method for solar cell material and device characterization. In *25th IEEE Photovoltaic Specialists Conference*, page 457, Washington, D.C., 1996.
- [41] Silke Steingrube, Pietro P. Altermatt, Daniel S. Steingrube, Jan Schmidt, and Rolf Brendel. Interpretation of recombination at c-Si/SiNx interfaces by surface damage. *Journal of Applied Physics*, 108(1):014506, 2010.
- [42] B Streetman and S Benerjee. *Solid State Electronic Devices*. 2010.
- [43] S.M Sze and K. NG Kwok. *Physics of Semiconductors*. Wiley, 3rd edition, 2007.
- [44] T. Trupke, R. A. Bardos, M. C. Schubert, and W. Warta. Photoluminescence imaging of silicon wafers. *Applied Physics Letters*, 89(4):44103–44107, 2006.
- [45] B van Zeghbroeck. MOS Capacitors. In *Principles of Semiconductor Devices*, chapter 6. 2011.
- [46] Eleonora Vella, Fabrizio Messina, Marco Cannas, and Roberto Boscaino. Unraveling exciton dynamics in amorphous silicon dioxide: Interpretation of the optical features from 8 to 11 eV. *Physical Review B*, 83(17):174201, May 2011.
- [47] H. a. Weakliem and D. Redfield. Temperature dependence of the optical properties of silicon. *Journal of Applied Physics*, 50(3):1491, 1979.
- [48] Kirt R Williams and Richard S Muller. Etch Rates for Micromachining Processing. *Journal of Microelectromechanical Systems*, 5(4):256–269, 1996.
- [49] U. Zaghoul, G. Papaioannou, F. Coccetti, P. Pons, and R. Plana. Dielectric charging in silicon nitride films for MEMS capacitive switches: Effect of film thickness and deposition conditions. *Microelectronics Reliability*, 49(9-11):1309–1314, September 2009.

Appendix

The following table shows the real refractive index (n) and the complex refractive index (k) of each of samples 1, 2 and 3 on the range $\lambda = 400 - 800\text{nm}$, as determined using VASE.

Wavelength [nm]	Sample 1		Sample 2		Sample 3	
	n	k	n	k	n	k
300	2.306	0.110	2.076	0.008	2.074	0.007
310	2.283	0.095	2.060	0.004	2.056	0.004
320	2.264	0.081	2.045	0.002	2.042	0.002
330	2.247	0.068	2.032	0.000	2.029	0.001
340	2.231	0.057	2.021	0.000	2.018	0.000
350	2.216	0.047	2.011	0.000	2.009	0.000
360	2.203	0.038	2.003	0.000	2.001	0.000
370	2.190	0.031	1.996	0.000	1.994	0.000
380	2.178	0.024	1.989	0.000	1.988	0.000
390	2.166	0.018	1.983	0.000	1.982	0.000
400	2.155	0.013	1.978	0.000	1.977	0.000
410	2.145	0.009	1.973	0.000	1.973	0.000
420	2.135	0.006	1.969	0.000	1.969	0.000
430	2.126	0.003	1.964	0.000	1.965	0.000
440	2.118	0.002	1.961	0.000	1.962	0.000
450	2.110	0.001	1.957	0.000	1.959	0.000
460	2.103	0.000	1.954	0.000	1.956	0.000
470	2.097	0.000	1.951	0.000	1.954	0.000
480	2.091	0.000	1.948	0.000	1.951	0.000
490	2.086	0.000	1.946	0.000	1.949	0.000
500	2.082	0.000	1.944	0.000	1.947	0.000
510	2.078	0.000	1.941	0.000	1.945	0.000
520	2.074	0.000	1.939	0.000	1.943	0.000
530	2.071	0.000	1.937	0.000	1.941	0.000
540	2.068	0.000	1.935	0.000	1.939	0.000
550	2.065	0.000	1.934	0.000	1.938	0.000
560	2.062	0.000	1.932	0.000	1.936	0.000
570	2.059	0.000	1.931	0.000	1.935	0.000
580	2.057	0.000	1.929	0.000	1.933	0.000
590	2.055	0.000	1.928	0.000	1.932	0.000
600	2.053	0.000	1.927	0.000	1.931	0.000
610	2.051	0.000	1.925	0.000	1.929	0.000

620	2.049	0.000	1.924	0.000	1.928	0.000
630	2.047	0.000	1.923	0.000	1.927	0.000
640	2.046	0.000	1.922	0.000	1.926	0.000
650	2.044	0.000	1.921	0.000	1.925	0.000
660	2.043	0.000	1.920	0.000	1.924	0.000
670	2.041	0.000	1.919	0.000	1.923	0.000
680	2.040	0.000	1.918	0.000	1.922	0.000
690	2.039	0.000	1.917	0.000	1.921	0.000
700	2.037	0.000	1.917	0.000	1.920	0.000
710	2.036	0.000	1.916	0.000	1.920	0.000
720	2.035	0.000	1.915	0.000	1.919	0.000
730	2.034	0.000	1.914	0.000	1.918	0.000
740	2.033	0.000	1.914	0.000	1.917	0.000
750	2.032	0.000	1.913	0.000	1.916	0.000
760	2.031	0.000	1.913	0.000	1.916	0.000
770	2.031	0.000	1.912	0.000	1.915	0.000
780	2.030	0.000	1.911	0.000	1.914	0.000
790	2.029	0.000	1.911	0.000	1.914	0.000
800	2.028	0.000	1.910	0.000	1.913	0.000
810	2.027	0.000	1.910	0.000	1.912	0.000
820	2.027	0.000	1.909	0.000	1.912	0.000
830	2.026	0.000	1.909	0.000	1.911	0.000
840	2.025	0.000	1.908	0.000	1.910	0.000
850	2.025	0.000	1.908	0.000	1.910	0.000
860	2.024	0.000	1.908	0.000	1.909	0.000
870	2.024	0.000	1.907	0.000	1.909	0.000
880	2.023	0.000	1.907	0.000	1.908	0.000
890	2.023	0.000	1.906	0.000	1.907	0.000
900	2.022	0.000	1.906	0.000	1.907	0.000
910	2.022	0.000	1.906	0.000	1.906	0.000
920	2.021	0.000	1.905	0.000	1.906	0.000
930	2.021	0.000	1.905	0.000	1.905	0.000
940	2.020	0.000	1.905	0.000	1.905	0.000
950	2.020	0.000	1.904	0.000	1.904	0.000
960	2.019	0.000	1.904	0.000	1.903	0.000
970	2.019	0.000	1.904	0.000	1.903	0.000
980	2.019	0.000	1.903	0.000	1.902	0.000
990	2.018	0.000	1.903	0.000	1.902	0.000
1000	2.018	0.000	1.903	0.000	1.901	0.000